



Spatio-temporal modelling of phenotypic heterogeneity in tumour tissues and its impact on radiotherapy treatment

Giulia L. Celora^{a,c,*}, Helen M. Byrne^a, P.G. Kevrekidis^b

^a Mathematical Institute, University of Oxford, Oxford, UK

^b Department of Mathematics & Statistics, University of Massachusetts, Amherst 01003, USA

^c Department of Mathematics, University College London, London, UK

ARTICLE INFO

Keywords:

Cancer stem cells
Radio-resistance
Heterogeneity

ABSTRACT

We present a mathematical model that describes how tumour heterogeneity evolves in a tissue slice that is oxygenated by a single blood vessel. Phenotype is identified with the stemness level of a cell and determines its proliferative capacity, apoptosis propensity and response to treatment. Our study is based on numerical bifurcation analysis and dynamical simulations of a system of coupled, non-local (in phenotypic “space”) partial differential equations that link the phenotypic evolution of the tumour cells to local tissue oxygen levels. In our formulation, we consider a 1D geometry where oxygen is supplied by a blood vessel located on the domain boundary and consumed by the tumour cells as it diffuses through the tissue. For biologically relevant parameter values, the system exhibits multiple steady states; in particular, depending on the initial conditions, the tumour is either eliminated (“tumour-extinction”) or it persists (“tumour-invasion”). We conclude by using the model to investigate tumour responses to radiotherapy, and focus on identifying radiotherapy strategies which can eliminate the tumour. Numerical simulations reveal how phenotypic heterogeneity evolves during treatment and highlight the critical role of tissue oxygen levels on the efficacy of radiation protocols that are commonly used in the clinic.

1. Introduction

In recent years, there has been a paradigm shift in how we understand cancer. New technologies, such as single-cell sequencing, have showcased the complex composition of tumours, where cells with different genotypes or phenotypes may coexist in the same tissue region (Black and McGranahan, 2021; Marusyk et al., 2012; Patel et al., 2014). While cancer was initially defined as a genetic disease, recent evidence suggests that phenotypic heterogeneity arises from both genetic and non-genetic sources of variability, such as epigenetic and environmental factors (Black and McGranahan, 2021; Cajal et al., 2020; Marusyk et al., 2020). Viewed through this lens, tumours are complex ecosystems in which competition and cooperation between cells, combined with environmental pressure, shape the system dynamics (Greaves and Maley, 2012; Marusyk et al., 2020) and response to treatment. Poor treatment outcomes have indeed been related to tumour heterogeneity (Dagogo-Jack and Shaw, 2018), with failure of therapies being associated with the presence and emergence of resistant phenotypes (Baliu-Piqué et al., 2020; Marusyk et al., 2020). Understanding the features that drive such heterogeneity is therefore important for the design of more effective treatment strategies (Baliu-Piqué et al., 2020; Cajal et al., 2020; Marusyk et al., 2020).

The concept of cancer stem cells (CSCs) was originally introduced to describe the hierarchical organisation of tumours, motivated by analogies with normal tissue development (Aponte and Caicedo, 2017; Greaves and Maley, 2012). While differentiated cells (DCs) have a finite clonogenic capacity, (i.e., after dividing a finite number of times they exit the cell-cycle and become terminally differentiated cells (TDCs)), CSCs can give rise to cells with the same clonogenic capacity when they divide. This capacity for self-renewal makes CSCs key drivers of tumour initiation, progression and relapse. The coexistence of CSCs, DCs and TDCs in tumours contributes to intra-tumour heterogeneity (Sousa et al., 2019), although in practice the heterogeneity is even richer, involving multiple types of CSCs, DCs and TDCs, blood vessels, immune and stromal cells. Here, we restrict attention to CSCs, DCs and TDCs. CSCs can drive heterogeneity and resistance via their ability to reversibly change their behaviour (such as metabolism and proliferation capacity) in order to survive toxic environmental conditions (such as, nutrient starvation or treatment) (Aponte and Caicedo, 2017; Fanelli et al., 2020; Sousa et al., 2019). Since such changes are heritable, CSCs can transmit such traits to their differentiated progeny and, thereby,

* Corresponding author.

E-mail address: celora@maths.ox.ac.uk (G.L. Celora).

drive the emergence of distinct clones (or lineages) of differentiated cells with different levels of resistance to treatment (Najafi et al., 2019).

Hypoxia, *i.e.*, abnormally low oxygen levels, is commonly found in solid tumours due to aberrant vascularisation (Höckel and Vaupel, 2001; Petrova et al., 2018). As oxygen diffuses into a tumour and is consumed by cells, spatial gradients in oxygen levels are established and regions of chronic or transient hypoxia may emerge. The clinical implications of hypoxia and its link to several hallmarks of cancer (Hanahan and Weinberg, 2000; Höckel and Vaupel, 2001; Ruan et al., 2009), such as evasion of apoptosis, genetic instabilities, induction of angiogenesis and metastasis, are well known. The response of cells to hypoxia is in part regulated by *hypoxia inducible factors* (HIFs) (Ruan et al., 2009), which can influence cancer cell metabolism, proliferation and “stemness” (a term that we use hereafter when referring to phenotypic variation of cancer cells). It has been shown that hypoxia facilitates the formation of stem-like cancer cells by up-regulating stem-related genes in a HIF-dependent manner (Axelson et al., 2005; Koh et al., 2011; Heddleston et al., 2010). *De novo* formation of CSCs can therefore occur in tumours in response to hypoxia-mediated stress (Pisco and Huang, 2015).

Mathematical models are a useful tool for studying the complex interplay between spatio-temporal variation in the tumour micro-environment and phenotypic heterogeneity, and its impacts on a tumour’s growth dynamics and response to treatment. The critical role of space in shaping tumour composition and/or treatment outcomes has been studied in previous works, where a wide range of mathematical formalisms has been used: from discrete agent based models (Bacevic et al., 2017; Bull et al., 2020; Damaghi et al., 2021; Noble et al., 2021; Scott et al., 2014; Strobl et al., 2022) to continuum models of different degrees of complexity (Astani and Preziosi, 2009; Frieboes et al., 2010; Greenspan, 1972; Lewin et al., 2020b; Villa et al., 2021). In particular, phenotype-structured models have proven useful for understanding intra-tumour phenotypic heterogeneity (Ardaševa et al., 2020; Chisholm et al., 2016, 2015; Fiandaca et al., 2021; Hodgkinson et al., 2019; Lorenzi et al., 2016; Lorz et al., 2015; Shen and Clairambault, 2020; Stace et al., 2020; Villa et al., 2021). These models comprise partial integro-differential equations in which changes in tumour heterogeneity are mediated by proliferation, competition and epigenetic mutations. Such frameworks have been used to understand how oxygen gradients shape metabolic heterogeneity (Fiandaca et al., 2021; Villa et al., 2021) as well as the consequences of resistance to chemotherapy (Lorenzi et al., 2018; Villa et al., 2020).

In our previous work (Celora et al., 2021), we developed a stemness-structured model to investigate how heterogeneity in stemness levels affects the growth dynamics of tumours in a well-mixed environment. In this model, a cell’s phenotypic state is described by a continuous variable, s , such that $s = 0$ corresponds to CSCs and $s = 1$ to TDCs. Furthermore, cells may change their state as a result of random and environment-driven epigenetic changes, which are represented, respectively, via diffusion and advection along the s -axis. When local oxygen levels are high, the advection flux favours differentiation; on the contrary, when oxygen levels are low the advection term favours de-differentiation, towards a stem-like phenotype. The differential effects of radiotherapy (RT) are also included by assuming that radio-sensitivity depends on the stemness level of the cells; in line with experimental evidence (Arnold et al., 2020; Diehn et al., 2009; Galeaz et al., 2021), CSCs are the most radio-resistant subpopulation. In this paper, we extend our earlier work to account for oxygen diffusion and consumption in the tumour and investigate how spatial variation in local oxygen levels affects the tumour’s phenotypic (*i.e.*, “stemness”) composition. Using a combination of numerical techniques, we find that the interplay between physical and phenotypic space gives rise to more complex dynamics than those observed in our earlier work (Celora et al., 2021). In particular, features of the spatial model, such as multistability and cusp bifurcations, disappear when spatial effects are neglected. We also investigate the combined effect of spatial and

phenotypic heterogeneity on radiation outcome. We use numerical simulations to compare the efficacy of different treatment strategies and, in particular, their ability to prevent CSC-driven relapse. In doing so, we provide insight into the role that dose fractionation and scheduling may play in preventing relapse.

The remainder of this paper is organised as follows. In Section 2 we present our stemness-structured spatially-resolved model and recast it in non-dimensional form. In Section 3, we present typical numerical simulations of the model, which highlight the influence of the initial conditions in determining the long-time behaviour of the system in the absence of treatment. The observed multistability of the model is further investigated in Section 4, where we numerically compute steady state solutions and employ continuation techniques to identify how equilibria and their linear stability change as key model parameters vary. In Section 5, we present dynamic simulations that illustrate how the ability of a tumour to successfully invade a tissue depends on its initial phenotypic composition. In Section 6, we investigate how specific model parameters dictate tumour responses to standard radiotherapy protocols. We find that the rate at which tumour cells consume oxygen plays a critical role in mediating their response to treatment, with high oxygen consumption rates (*i.e.*, larger variation in the oxygen levels across the tumour tissue) correlating with poor outcomes. Furthermore, we discuss how adapting RT scheduling can improve treatment efficacy. In Section 7, we summarise our findings and outline future research directions. The appendices contain details about the numerical methods, the parameter values and the bifurcation analysis.

2. Model development

We consider a fixed tissue region in which oxygen is supplied by blood vessels located on the domain boundaries (see Fig. 1). For simplicity, we consider a 1D Cartesian domain of length $2L$ and assume that the model variables depend on the spatial location x [mm], where $x \in [-L, L]$, and time t [days]. The state of a tumour cell in phenotypic space is described by its stemness level s (we view s as a dimensionless independent variable with $0 \leq s \leq 1$); stemness levels influence a cell’s proliferation capacity, its response to treatment (here radiotherapy) and physiological stresses (here hypoxia). We denote by $N = N(x, s, t)$ [cells mm⁻¹] the number of tumour cells with phenotype s , at spatial location x and time t . We denote by $\Phi = \Phi(x, t)$ [cells mm⁻¹] the total number of tumour cells at location x and time t :

$$\Phi(x, t) = \int_0^1 N(x, s, t) ds, \quad (1)$$

while the total tumour burden (*i.e.*, the total number of tumour cells in the slice of tissue) is denoted as $M = M(t)$ [cells]:

$$M(t) = \int_{-L}^L \Phi(x, t) dx. \quad (2)$$

The evolution of N is dictated by cell proliferation and death as well as spatial ($J_x = J_x(x, s, t)$) and phenotypic ($J_s = J_s(x, s, t)$) fluxes along the x and s axes, respectively. Cell behaviour is also influenced by local levels of oxygen $C = C(x, t)$ [mmHg]. As oxygen diffuses into the tissue, it is consumed by cells at a rate that may depend on their phenotype, causing different oxygen environments, or *niches*, to form. Under these assumptions, we have that the time evolution of N and C is determined by the following system of coupled non-linear and non-local parabolic partial differential equations (PDEs):

$$\frac{\partial N}{\partial t} + \frac{\partial J_x}{\partial x} + \frac{\partial J_s}{\partial s} = F(s, C, \Phi, t)N, \quad (3a)$$

$$\frac{\partial C}{\partial t} = D_{xc} \frac{\partial^2 C}{\partial x^2} - \underbrace{\int_0^1 \Gamma(s, C)N(x, s, t) ds}_{\text{net oxygen consumption}}. \quad (3b)$$

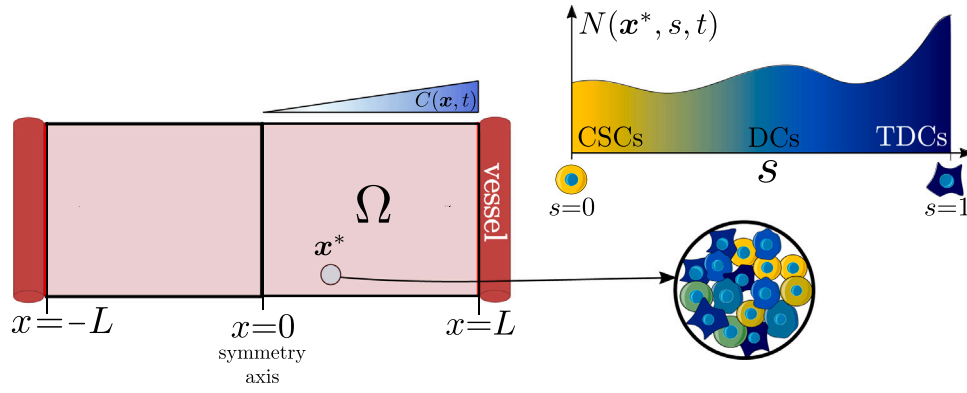


Fig. 1. Schematic representation of the model structure: we consider a fixed slice of tissue delimited by two vessels at location $x = \pm L$. We reduce the model to a 1D Cartesian geometry by assuming that there is no spatial variation in the y direction. Tumour cells in the domain are characterised by their stemness level s : $s = 0$ corresponds to fully stem-like cells while $s = 1$ to cells that are terminally differentiated. At each spatial location x^* the density of cells with phenotype s is denoted by $N(x^*, s, t)$ and its time evolution is described by the system (3).

In Eq. (3b), the positive constant D_{xc} [$\text{mm}^2 \text{hr}^{-1}$] is the diffusion coefficient of oxygen and the function $\Gamma = \Gamma(s, C)$ [$\text{mmHg}/(\text{cell h})^{-1}$] represents the rate at which cells of phenotype s consume oxygen. Following Fiandaca et al. (2021), Villa et al. (2021), we assume further that cells move randomly in space, in which case the spatial flux J_x is given by:

$$J_x = -D_{xn} \frac{\partial N}{\partial x}, \quad (3c)$$

where the positive constant D_{xn} [$\text{mm}^2 \text{hr}^{-1}$] represents the diffusion coefficient of cells in physical space. We note that alternative functional forms could be used to model tumour cell movement. For example, the diffusion coefficient may depend non-linearly on the phenotypic distribution, N . Alternatively, higher-order derivatives (or/and cross-diffusion terms) may be considered when defining the diffusive flux (Cohen and Murray, 1981; Lima et al., 2017). We postpone discussion of alternative modelling approaches that give rise to non-linear diffusion to the conclusions. Motivated by existing models (Chisholm et al., 2015; Hodgkinson et al., 2019), we suppose that the phenotypic flux J_s comprises two terms: one due to random epigenetic mutations and one due to changes in cell stemness that are mediated by environmental cues. These processes are represented, respectively, via diffusion and advection terms so that J_s is given by:

$$J_s = -D_{sn} \frac{\partial N}{\partial s} + V_s(s, C)N. \quad (3d)$$

Here, the positive constant D_{sn} [hr^{-1}] represents the rate at which random epigenetic mutations take place, while the velocity $V_s = V_s(s, C)$ [hr^{-1}] describes the rate at which cells of phenotype s alter their stemness level in response to local oxygen levels.

Focusing on the right-hand side of Eq. (3a), the function $F = F(s, C, \Phi, t)$ [hr^{-1}] describes the net rate of cell proliferation, defined as the difference between the cell proliferation and death rates. As such, it also captures the effect of radiotherapy, which we assume to be administered in Z doses d_i [Gy] at discrete times t_i ($i = 1, \dots, Z$). Under these assumptions, we define F as:

$$F(s, C, \Phi, t) = \underbrace{P_e(s, C, \Phi)}_{\text{proliferation}} - \underbrace{K(s, C)}_{\text{cell death}} - \underbrace{\sum_{i=1}^Z \log\left(\frac{1}{S_{RT}(s, C, P_e; d_i)}\right) \delta(t - t_i)}_{\text{radiotherapy}}, \quad (3e)$$

$$\text{where } P_e(s, C, \Phi) = P(s, C) \left(1 - \frac{\Phi}{\Phi_{max}}\right). \quad (3f)$$

In Eq. (3e), we assume that cells proliferate at a rate $P_e = P_e(s, C, \Phi)$ [day^{-1}] as defined in Eq. (3f), where the function $P(s, C)$ indicates the

cell proliferation rate in the absence of competition (i.e., $\Phi = 0$), while the logistic-type term captures growth inhibition due to competition for space. Here Φ_{max} [cells/mm] represents the local carrying capacity of the tissue (so that if $\Phi(x, 0) \in [0, \Phi_{max}]$ then $\Phi(x, t) \in [0, \Phi_{max}]$ for $t \geq 0$). Cells die at a rate $K = K(s, C)$ [day^{-1}] which is modulated by the stemness levels s and the local oxygen levels C . The final sink term in Eq. (3e) is associated with cell death due to radiotherapy (RT); here $S_{RT} = S_{RT}(s, C, P_e; d_i) \in [0, 1]$ denotes the fraction of cells that survive exposure to a dose d_i of RT. We here use the term $\log(1/S_{RT})$ to model cell death due to RT although other forms have been proposed. For example, in Lewin et al. (2020a), the term $(1 - S_{RT})$ is used. The improved accuracy of the logarithmic functional form was argued in Celora et al. (2021). In writing Eq. (3e), we assume that radiotherapy results in instantaneous cell death. In other words, we assume that RT-mediated cell death occurs on a much faster time scale than the reference time scale considered in the model (i.e., the time scale of cell proliferation). We note that, in practice, RT does not always result in instantaneous cell death; it may induce delayed cell-death or senescence where cells permanently withdraw from the cell-cycle but remain viable (Sia et al., 2020). For simplicity, and in line with other existing models (e.g., Lewin et al., 2020a; Rockne et al., 2008), we neglect such possibilities and postpone their consideration to future work.

In line with the geometry presented in Fig. 1, we impose the following boundary conditions:

$$D_{sn} \frac{\partial N}{\partial s} - NV_s \Big|_{s \in \{0,1\}} = 0, \quad x \in [-L, L], t > 0, \quad (3g)$$

$$\frac{\partial N}{\partial x} \Big|_{x = \pm L} = 0, \quad s \in [0, 1], t > 0, \quad (3h)$$

$$C(\pm L, t) = C_\infty, \quad t > 0. \quad (3i)$$

Eqs. (3g)–(3h) state that the phenotypic and spatial fluxes of the cells vanish on the relevant domain boundaries. In Eq. (3i), the supply of oxygen (from vessels at tissue boundaries) is modelled by prescribing a constant oxygen concentration, C_∞ , on $x = \pm L$. Finally, we close the governing equations by imposing the following initial conditions:

$$N(x, s, 0) = N_0(x, s) \quad x \in [-L, L], s \in [0, 1], \quad (3j)$$

$$C(x, 0) = C_0(x) \quad x \in [-L, L], \quad (3k)$$

where $N_0(x, s)$ and $C_0(x)$ are non-negative functions.

We now recast the model in dimensionless form. We choose the following scalings for the model variables

$$\tau = \frac{t}{\tau_0}, \quad X = \frac{x}{L}, \quad n = \frac{N}{\Phi_{max}}, \quad \phi = \frac{\Phi}{\Phi_{max}}, \quad (4)$$

$$c = \frac{C}{C_\infty}, \quad m = \frac{M}{2\Phi_{max}}.$$

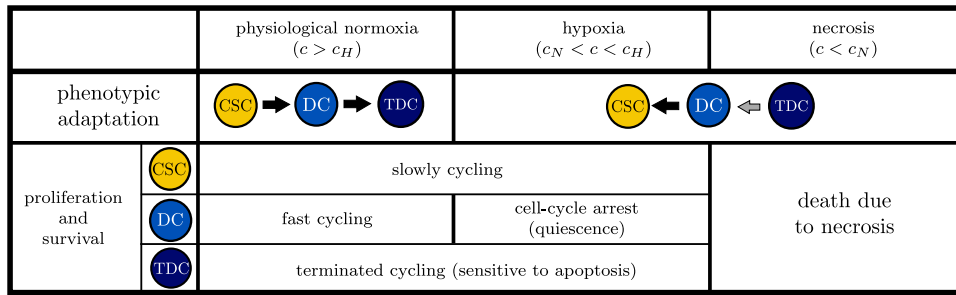


Fig. 2. Schematic representing how oxygen affects cell phenotype (via inducing adaptation) and other cell functions (proliferation and death). Values associated with the oxygen thresholds c_H and c_N can be found in Table B.2.

where τ_0 is a positive constant which indicates the time scale of interest. Here we want to resolve the growth dynamics of the tumour, which usually occur on the timescale of days; for this reason we set $\tau_0 = 1$ day as a representative value.

Substituting (4) into Eqs. (3) and exploiting the assumed symmetry about $X = 0$, we deduce that the evolution of the re-scaled cell distribution $n = n(X, s, \tau)$ is governed by

$$\frac{\partial n}{\partial \tau} = D_{xn} \frac{\partial^2 n}{\partial X^2} + \frac{\partial}{\partial s} \left(D_{sn} \frac{\partial n}{\partial s} - v_s(s, c)n \right) + F(s, c, \phi, \tau)n, \quad (X, s) \in (0, 1)^2, \tau > 0, \tag{5a}$$

$$D_{sn} \frac{\partial n}{\partial s} - nv_s \Big|_{s=0,1} = 0, \quad X \in [0, 1], \tau > 0, \tag{5b}$$

$$\frac{\partial n}{\partial X} \Big|_{X=0,1} = 0, \quad s \in [0, 1], \tau > 0, \tag{5c}$$

$$n(X, s, 0) = n_0(X, s), \quad X \in [0, 1], s \in [0, 1], \tag{5d}$$

where

$$\phi(X, \tau) = \int_0^1 n(X, s, \tau) ds, \tag{5e}$$

$$F(s, c, \phi, \tau) = P_e(s, c, \phi) - \mathcal{K}(s, c) - \sum_{i=1}^Z \log \left(\frac{1}{S_{RT}(s, c, P_e; d_i)} \right) \delta \left(\tau - \frac{t_i}{\tau_0} \right), \tag{5f}$$

$$P_e(s, c, \phi) = P(s, c)(1 - \phi), \tag{5g}$$

and the rescaled total tumour burden m reads:

$$m(\tau) = \int_0^1 \phi(X, \tau) dX. \tag{5h}$$

The evolution of the normalised oxygen concentration c satisfies

$$\frac{\partial c}{\partial \tau} = D_{xc} \frac{\partial^2 c}{\partial X^2} - \int_0^1 \gamma(s, c)n(X, s, t) ds, \quad X \in (0, 1), t > 0, \tag{6a}$$

$$c(1, t) = 1, \quad \frac{\partial c}{\partial X}(0, t) = 0, \quad t > 0, \tag{6b}$$

$$c(x, 0) = c_0(x), \quad X \in [0, 1]. \tag{6c}$$

In Eqs. (5)–(6), we have introduced the following dimensionless parameter groupings and functional forms:

$$\begin{aligned} D_i &= \frac{D_i \tau_0}{L^2}, \quad i \in \{xn, xc\}, \\ \gamma(s, c) &= \frac{\Gamma(s, c C_\infty) \Phi_{max} \tau_0}{C_\infty}, \\ v_s(s, c) &= V_s(s, c C_\infty) \tau_0, \\ P_e(s, c, \phi) &= P_e(s, c C_\infty, \phi \Phi_{max}) \tau_0, \\ P(s, c) &= P(s, c C_\infty) \tau_0, \\ \mathcal{K}(s, c) &= K(s, c C_\infty) \tau_0, \\ F(s, c, \phi, T) &= F(s, c C_\infty, \phi \Phi_{max}, \tau \tau_0) \tau_0, \\ S_{RT}(s, c, P_e; d_i) &= S_{RT}(s, c C_\infty, P_e \tau_0; d_i). \end{aligned} \tag{7}$$

Based on standard values reported in the literature (see Table B.2) and considering a tissue region that is several micrometres wide ($L \approx 200 \mu\text{m}$), we find that $D_{xc} \gg 1$. This is because the time scale of oxygen diffusion in the tumour region ($L^2 D_{xc}^{-1}$) is of the order of minutes, which is much faster than the characteristic time scale τ_0 of tumour growth. We exploit this separation of timescales to simplify the numerical simulations for which we assume that the oxygen distribution is in quasi-equilibrium, so that c satisfies

$$D_{xc} \frac{\partial^2 c}{\partial X^2} - \int_0^1 \gamma(s, c)n(X, s, t) = 0, \quad c(1, t) = 1, \quad \frac{\partial c}{\partial X}(0, t) = 0. \tag{8}$$

Under this quasi-steady approximation, which is common in mathematical models of tumour growth (Bull et al., 2020; Lewin et al., 2020b), the oxygen spatial distribution quickly adapts to changes in the tumour composition. As a result, it is not necessary to impose initial conditions on c .

2.1. Specification of functional forms

We now define the functional forms of v_s , P , \mathcal{K} , γ and S_{RT} . Some are similar to those used in Celora et al. (2021) where we studied the spatially well-mixed counterpart of Eqs. (5) and (8).

A key feature of the model is the role of oxygen levels in determining cell behaviour. We assume that the tumour can be subdivided into three niches according to local oxygen levels: physiological normoxia ($c_H < c < 1$), hypoxia ($c_N < c < c_H$) and necrosis ($0 \leq c < c_N$). In Fig. 2, we show how cells with different stemness levels behave in these niches.

We suppose that the proliferation rate \mathcal{P} in Eq. (5f) takes the following form:

$$P(s, c) = p_{CSC}(c) \exp[-\Psi_{CSC}(s)^2] + p_{DC}(c) \exp[-\Psi_{DC}(s)^2], \tag{9a}$$

$$\text{where } p_i(c) = p_i^{max} \frac{c^4}{K_i^4 + c^4}, \quad \Psi_i(s) = \frac{s - s_i}{g_i}, \quad i \in \{CSC, DC\}. \tag{9b}$$

In Eq. (9a)–(9b), a bimodal function describes the proliferation rate P ; the two peaks correspond to CSCs ($s_{CSC} = 0$) and differentiated cells (DCs) ($s_{DC} = 0.55$) which proliferate at rates $p_{CSC}(c)$ and $p_{DC}(c)$ respectively. We assume further that both p_{CSC} and p_{DC} are increasing, saturating functions of c (see Eq. (9b)). Based on what has been reported in the literature (Dhawan et al., 2016; Hoffmann et al., 2008), we assume that in physiological oxygen conditions ($c \approx 1$) DCs proliferate at a faster rate than CSCs (i.e., $p_{CSC}^{max} = \delta_p p_{DC}^{max}$ with $\delta_p < 1$). Due to the higher plasticity of CSCs, the latter are thought to adapt more readily to hypoxia so that they can continue to proliferate, even in low oxygen environments (Chae and Kim, 2018; Garnier et al., 2019; Snyder et al., 2018). In line with these observations, we assume that $K_{CSC} < K_{DC}$ so that CSCs proliferate faster than DCs in low oxygen environments.

We assume that the death rate $\mathcal{K} = \mathcal{K}(s, c)$ in Eq. (5f) takes the following form:

$$\mathcal{K}(s, c) = \underbrace{d_{TDC} \exp \left[- \left(\frac{1-s}{g_{TDC}} \right) \right]}_{\text{natural cell death}} + \underbrace{d_n H_{\epsilon_k}(c_N - c)}_{\text{necrosis}}, \tag{9c}$$

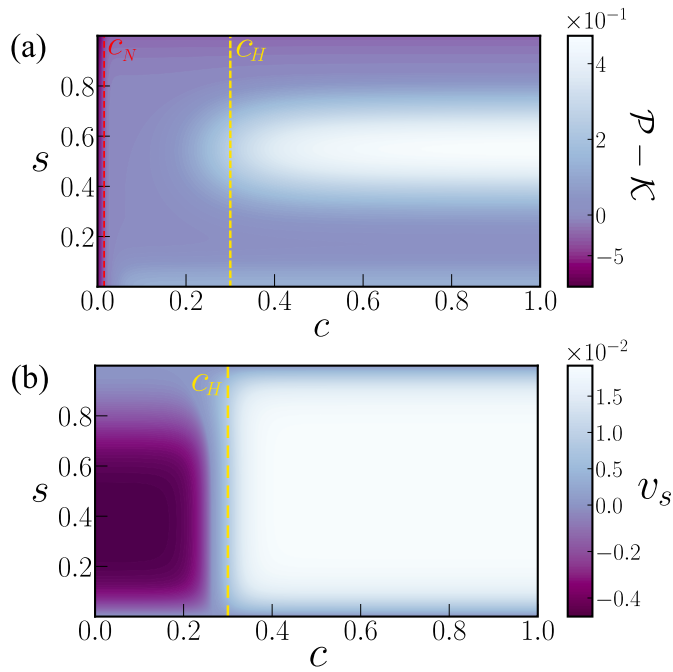


Fig. 3. Surface plots of the functional (a) $\mathcal{P}(s,c) - \mathcal{K}(s,c)$ defined by Eqs. (9a)–(9c) and (b) $v_s(s,c)$ defined by Eq. (10). To generate these surface plots we used the parameters listed in Table B.2.

$$\text{where } H_\epsilon(x) = \frac{1}{2} + \frac{1}{2} \tanh(x\epsilon^{-1}). \quad (9d)$$

In Eq. (9c), we account for two mechanisms of cell death: natural cell death and necrosis. Natural cell death is assumed to be independent of oxygen levels c and to affect only TDCs ($s \approx 1$). By contrast, necrosis is assumed to impact all cells, regardless of their stemness level s , but only when oxygen levels are extremely low ($c \lesssim c_N \ll 1$). We denote by H_ϵ the continuous step function; here, the parameter ϵ determines how rapidly H_ϵ switches between its extremal values ($H_\epsilon(x) \approx 1$ for $x > \epsilon$ and $H_\epsilon(x) \approx 0$ for $x < -\epsilon$). In Eq. (9c), we suppose that the transition between the hypoxic and necrotic niches is rapid and, hence, we fix $\epsilon_k = 0.01$. In Fig. 3(a), we plot the net proliferation rate (i.e., $\mathcal{P} - \mathcal{K}$), and show how it depends on the local oxygen levels (c) and phenotype (s).

As illustrated in Fig. 2, we assume that cells differentiate (i.e., $v_s > 0$) in physiological conditions ($c > c_H$) and that they dedifferentiate and assume stem-like traits (i.e., $v_s < 0$) under hypoxia ($c < c_H$) (Picco et al., 2017). Following Celora et al. (2021), we adopt the following functional form for the phenotypic advection velocity v_s :

$$v_s(s,c) = v_s^+(s)H_{\epsilon_v}(c - c_H) - v_s^-(s)H_{\epsilon_v}(c_H - c), \quad (10a)$$

where

$$v_s^+(s) = \frac{V_+}{V_+^*} \tanh\left(\frac{s^{\omega_+}}{\xi_+}\right) \tanh\left(\frac{1-s}{\xi_+}\right), \quad (10b)$$

and

$$v_s^-(s) = \frac{V_-}{V_-^*} \tanh\left(\frac{s}{\xi_-}\right) \tanh\left(\frac{(1-s)^{\omega_-}}{\xi_-}\right). \quad (10c)$$

In Eqs. (10b)–(10c), the normalising factors V_\pm^* are defined so that $\max_{s \in [0,1]}(v_s^\pm) = V_\pm^*$, where V_\pm correspond to the maximum absolute values of the velocities with which cells differentiate (V_+) and dedifferentiate (V_-). The positive constants ξ_\pm determine how rapidly the velocity profiles switch near $s = 0$ and $s = 1$. The exponents ω_\pm are positive integers: $\omega_+ = 1$ and $\omega_- = 2$ (this choice is based on analysis performed in Celora et al. (2021)). We assume the transition

between positive and negative advection velocities occurs at the threshold oxygen level c_H . This transition is incorporated via the smooth function H_{ϵ_v} , as defined in Eq. (9d), with $\epsilon_v = 0.05$. The profile for v_s is illustrated in Fig. 3(b).

To complete our model for tumour growth in the absence of treatment, we must specify the functional form for $\gamma = \gamma(s,c)$ in Eq. (8). While we expect oxygen consumption to depend on the stemness variable s , in the absence of suitable experimental data with which to define this dependence, we follow Scott et al. (2014) and assume $\gamma = \gamma(c)$. Furthermore, following Greenspan (1972), Lewin et al. (2020b), we suppose that γ falls rapidly to zero when oxygen levels drop below the necrotic threshold $c = c_N$ and, hence, we write:

$$\gamma = \gamma_0 H_{\epsilon_\gamma}(c - c_N). \quad (11)$$

In Eq. (11), the positive constant γ_0 represents the value of the ratio of the characteristic time scale for tumour cell proliferation, τ_0 , and the time scale on which tumour cells consume oxygen. We fix $\epsilon_\gamma = 0.05$.

The survival fraction. Cell sensitivity to radiotherapy is affected by environmental conditions, such as oxygen levels (Sørensen and Horsman, 2020; Suwa et al., 2021), as well as cell-intrinsic factors, such as phenotype (Arnold et al., 2020; Galeaz et al., 2021; Syljuåsen, 2019; Tang et al., 2018). To account for heterogeneity in tumour cell responses to RT, we augment the standard linear–quadratic model by assuming that the fraction of cells with phenotype s , exposed to oxygen levels c , and proliferating at a rate \mathcal{P}_e , that survives a single dose d of RT is given by McMahon (2018):

$$\ln(S_{RT}(s,c,\mathcal{P}_e;d)) = -\alpha(s,c,\mathcal{P}_e)d - \beta(s,c,\mathcal{P}_e)d^2, \quad (12a)$$

where $\alpha[\text{Gy}^{-1}]$ and $\beta[\text{Gy}^{-2}]$ are positive functions.

We assume that three mechanisms contribute to radio-resistance: (1) local oxygen levels, (2) stemness and, (3) quiescence (i.e., transient cell-cycle arrest). These effects are incorporated by decomposing α (and, analogously, β) into three factors, each accounting for one resistance mechanism:

$$\alpha(s,c,\mathcal{P}_e) = \alpha_1(c)\alpha_2(s)\alpha_3(\mathcal{P}_e), \quad \beta(s,c,\mathcal{P}_e) = \beta_1(c)\beta_2(s)\beta_3(\mathcal{P}_e). \quad (12b)$$

First, it is well known that low oxygen levels can adversely impact radiotherapy efficacy; oxygen is an essential reactant for the fixation of radio-induced DNA damage and subsequent cell death (Wenzl and Wilkens, 2011; McMahon, 2018; Sørensen and Horsman, 2020; West and Slevin, 2019). This effect is typically incorporated into the survival fraction via the oxygen enhancement ratio (OER) (Lewin et al., 2020a; Wenzl and Wilkens, 2011). The OER is the ratio of the radiation doses that should be given in anoxia and normoxia to achieve the same biological effect (i.e., the same overall survival fraction) (Wenzl and Wilkens, 2011); the OER of tumours usually ranges between 1 and 4. As in Lewin et al. (2020a), we assume that the OER only plays a role under radio-biological hypoxia (i.e., where $c \leq c_R$), and propose the following functional forms for $\alpha_1(c)$ and $\beta_1(c)$:

$$\alpha_1(c) = \begin{cases} 1, & c > c_R \\ \text{OER}^{-1}, & c \leq c_R, \end{cases} \quad \beta_1(c) = \begin{cases} 1, & c > c_R \\ \text{OER}^{-2}, & c \leq c_R \end{cases} \quad (12c)$$

where the threshold c_R is such that $c_N < c_R < c_H$ (see Table B.2 for quantitative estimates). As in Celora et al. (2021), we account for the intrinsic radio-resistance of CSCs (Arnold et al., 2020; Diehn et al., 2009; Galeaz et al., 2021; Olivares-Urbano et al., 2020) by proposing the following functional forms for $\alpha_2(s)$ and $\beta_2(s)$:

$$\alpha_2(s) = \alpha_- + \Delta\alpha \tanh(\kappa s), \quad \beta_2(s) = \beta_- + \Delta\beta \tanh(\kappa s), \quad (12d)$$

In Eq. (12d), the positive constants α_- and β_- represent the radio-sensitivity of CSCs (i.e., $s \approx 0$) while $\Delta\alpha > 0$ and $\Delta\beta > 0$ denote the increase in radio-sensitivity between CSCs and more differentiated cell phenotypes. The constant κ determines how rapidly sensitivity to RT changes with phenotype. We choose κ so that α_2 and β_2 are maximal for

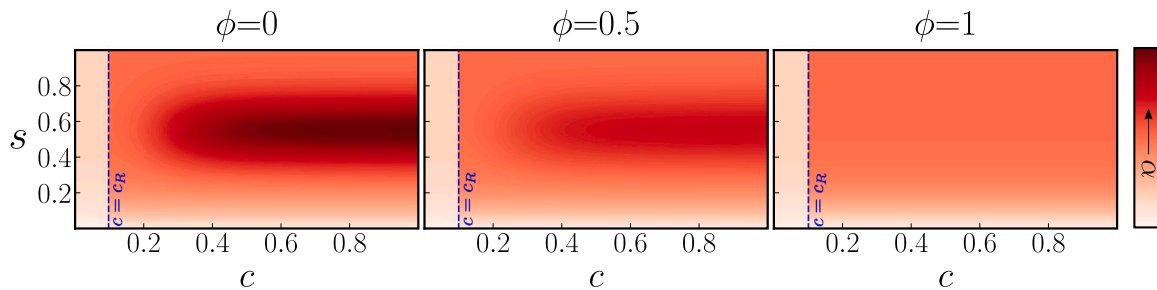


Fig. 4. Series of plots showing how, for fixed value of ϕ , $\alpha = \alpha(s, c, \phi)$ (defined by Eq. (12a)) changes as the phenotypic variable s and the oxygen concentration c vary. We plot α for different values of the rescaled cell density ϕ to show also how competition for space modulates the radio-sensitivity. Parameter values set as in Tables B.1–B.2.

$s \gtrsim 0.5$. Finally, the terms α_3 and β_3 are included in order to account for the increased sensitivity to RT of rapidly proliferating cells compared to growth-arrested cells (Barendsen et al., 2001; Enderling et al., 2009; Franken et al., 2013):

$$\alpha_3(\mathcal{P}_e) = \beta_3(\mathcal{P}_e) = \left(1 + \frac{\mathcal{P}_e(s, C, \phi)}{\mathcal{P}_{max}}\right). \quad (12e)$$

In Eq. (12e), $\mathcal{P}_{max} = \max_{c,s,\phi} \mathcal{P}_e = p_{DC}^{max}$.

The combined effect of the three radio-resistance mechanisms is illustrated in Fig. 4 (we show plots of α only since β has a qualitatively similar behaviour). When oxygen levels drop below c_R (see blue dashed line in Fig. 4), the cells' radio-sensitivity falls. For milder levels of hypoxia (e.g., $c_R < c < c_H$), cell proliferation is inhibited for all phenotypes s so that the dominant mechanism modulating radio-sensitivity is the intrinsic radio-sensitivity of the cells (i.e., $\alpha \sim \alpha_2(s)$). Spatial competition is relevant at higher oxygen concentration (e.g., $c > c_H$). Where spatial competition is low ($\phi \approx 0$), differentiated cells ($s \approx 0.5$) are highly radio-sensitive; by contrast, TDCs are less sensitive as they are not proliferating. However, when competition for space inhibits cell proliferation TDCs and DCs respond similarly to radiotherapy. We note that, in our model, the overall radio-sensitivity depends on the tumour's composition as well as the local environment, both of which can evolve over time and change in response to treatment.

2.2. Numerical methods and interpretation of the numerical simulations

Dynamic simulations. We use the method of lines to solve the time-dependent system given by Eqs. (5) and (8). In more detail, we use finite volume and central finite differences respectively to discretise the phenotypic (s) and spatial (X) derivatives in Eqs. (5) and (8). We advance Eq. (5a) by adopting an implicit, multi-step time-stepping method, based on backward differentiation formulae (BDF), which is suitable for stiff equations. Given the discrete form of the solution $n(s, X, \tau)$ at time τ , we then compute $\phi(X, \tau)$. We use the latter to solve Eq. (8) for the oxygen concentration c , via a fixed point iteration method. A detailed description of the numerical method and relevant references are included in Appendix A.

We initialise the simulations by assuming that, at $t = 0$, the cells are distributed uniformly in space and normally along the stemness axis, with mean stemness $s_0 \in (0, 1)$ and variance $\sigma_s > 0$. Thus, we prescribe

$$n(s, X, \tau = 0) = n_0(s, X) = \frac{m_0}{\sqrt{2\pi\sigma_s}} \exp\left[-\frac{(s - s_0)^2}{2\sigma_s^2}\right], \quad (13)$$

where $m_0 > 0$ is the initial tumour burden, while s_0 and σ_s are chosen so that the mass of the Gaussian profile lies inside the stemness domain $s \in (0, 1)$ and the Neumann boundary conditions (5b) are satisfied, up to a negligible (exponentially small) correction. In all our simulations, unless otherwise stated, model parameters are fixed at the default values listed in Tables B.1–B.2; where possible these values are taken from the literature and are relevant to prostate cancer.

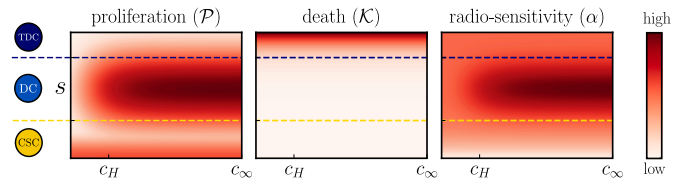


Fig. 5. Illustration of the relationship between the definition of the three discrete subpopulation, (CSCs, DCs and TDCs) and the cells maximum proliferation potential (i.e., \mathcal{P}), natural death (i.e., \mathcal{K}) radio-sensitivity (i.e., α). The yellow and blue dotted line indicate, respectively $s = s_1 = 0.3$ and $s = s_2 = 0.8$.

Numerical bifurcation analysis. In Section 4, we investigate equilibrium solutions of Eqs. (5)–(6) or parameter values Tables B.1–B.2 by leveraging numerical continuation techniques. Specifically, we use Julia's package BifurcationKit (Veltz, 2020) to compute stationary solutions (stable and unstable ones), study their stability and identify bifurcation points (BifurcationKit is an open-source software package for computing bifurcation diagrams). More details are included in Appendix A. We note that, in Section 4, we present all of the positive steady states that were numerically identified. These solutions were also the only ones observed in dynamic numerical simulations; however we cannot, a priori, exclude the possibility that other stationary solutions, not detected by our analysis, or other type of attractors (such as limit cycles) might exist.

Interpretation of the numerical results. Our model describes cell phenotypes via a continuous stemness axis. To reconcile this description with the standard discrete classification of cells into cancer stem cells (CSCs), differentiated cells (DCs) and terminally differentiated cells (TDCs), we subdivide the stemness axis s into three intervals that map to each subpopulation. As shown in Fig. 5, the subdivision is based on the cells' proliferative capacity (\mathcal{P}) and their sensitivity to natural cell death (\mathcal{K}) and radiotherapy (α and β). CSCs ($s_{CSC}^0 \leq s \leq s_{CSC}^1$) are highly radio-resistant and stem-like, while DCs ($s_{DC}^0 < s \leq s_{DC}^1$) are highly proliferative and radio-sensitive. Finally, TDCs ($s_{TDC}^0 < s \leq s_{TDC}^1$) have a high death rate \mathcal{K} . Without loss of generality, we fix $s_{CSC}^0 = 0$, $s_{CSC}^1 = s_{DC}^0 = 0.3$, $s_{DC}^1 = s_{TDC}^0 = 0.8$ and $s_{TDC}^1 = 1$. We emphasise that this classification is not a "firm distinction"; the thresholds s_z^0 and s_z^1 ($z \in \{CSC, DC, TDC\}$) are chosen arbitrarily to simplify presentation of the numerical results and small changes in their values do not significantly affect the results. For each subpopulation, we define the local cell fractions $\pi_z = \pi_z(X, \tau)$:

$$\pi_z(X, \tau) = \frac{1}{m(\tau)} \int_{s_z^0}^{s_z^1} n(X, s, \tau) ds, \quad z \in \{CSC, DC, TDC\}. \quad (14)$$

The metrics π_z are informative when studying the phenotypic composition in the different niches that form within the tumour as a result of spatial heterogeneity in oxygen levels. When considering, instead, the tumour as a whole, we focus on the overall cell fraction $\Pi_z = \Pi_z(t)$:

$$\Pi_z(\tau) = \frac{1}{m(\tau)} \int_0^1 \pi_z(X, \tau) dX, \quad z \in \{CSC, DC, TDC\}. \quad (15)$$

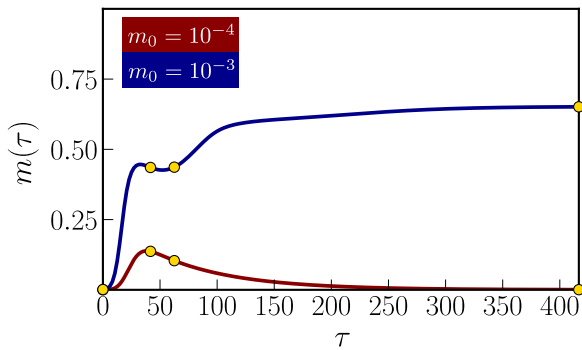


Fig. 6. Evolution of the tumour burden for two different initial conditions (but same model parameters) illustrating the model allows for multiple stable steady states. Numerical results generated by solving the full model, defined by Eqs. (5), (8)–(11) and (13), with $s_0 = 0.5$ and two values of m_0 . We run the simulation up to time $\tau = 420$, corresponding to ≈ 60 weeks. All other model parameters are fixed at the default values specified in Tables B.1–B.2, with $\gamma_0 = 4D_{sc}$. When $m_0 = 10^{-3}$ (blue curve), the tumour persists and eventually evolves to a non-trivial steady state; when the initial tumour burden is decreased ($m_0 = 1e^{-4}$, red curve), the tumour grows initially but at long times becomes extinct. The yellow dots indicate the time points at which the snapshots in Fig. 7 are taken.

We note that the three fractions are not independent since, by definition, $\Pi_{CSC}(t) + \Pi_{DC}(t) + \Pi_{TDC}(t) \equiv 1$.

3. Dynamics in the absence of treatment

We start our analysis by presenting dynamic simulations of our tumour growth model, in the absence of treatment. In Fig. 6, we show how the tumour burden, $m(t)$, evolves for two simulations in which all parameter values are the same except for the initial tumour burden, m_0 . When m_0 is sufficiently large (e.g., $m_0 = 10^{-3}$), the tumour invades the tissue; for smaller values of m_0 (e.g., $m_0 = 10^{-4}$) the tumour becomes extinct (see also Fig. 7). These results highlight one of the key features of our model: multi-stability. Interestingly, while the long-time behaviours of $m(\tau)$ for these two initial conditions are different, their short-time dynamics (until $\tau \approx 50$) are qualitatively similar. In both cases, the tumour grows until $\tau \approx 41$ (6 weeks) when m starts to decrease. Thereafter, the size of tumour with the smaller initial burden decreases monotonically towards extinction, while the tumour with the larger initial burden resumes growth and eventually attains a non-trivial steady state.

To understand why the dynamics diverge, we consider the time evolution of the cell distribution $n(X, s, \tau)$ (see Fig. 7). In both cases, the tumour initially comprises differentiated cells that proliferate rapidly and, thus, the tumour burden $m(\tau)$ increases. Over time, as these cells proliferate, they differentiate so that when $\tau = 41$ (≈ 6 weeks), the tumour is composed primarily of TDCs (note the large values of $n(X, 1, \tau)$ in Figs. 7(a.2) and 7(b.2)). Since the net proliferation rate of TDCs is negative, $m(\tau)$ starts to decrease. Even though these TDCs do not proliferate, they consume oxygen. Consequently, if sufficiently many TDCs are present, a hypoxic region forms at the tumour centre (where $x \approx 0$; see Fig. 7(b.2)). In the hypoxic niche, cell differentiation slows down and, if oxygen levels are sufficiently low, cells de-differentiate. The different signals experienced by tumour cells in the normoxic and hypoxic niches select for different phenotypes and drive spatial variation in the tumour's phenotypic composition which is amplified over time (compare the cell distributions in Figs. 7(b.2) and 7(b.4), for example). By contrast, in Fig. 7(a.2), there are so few TDCs that oxygen levels remain above the hypoxic threshold, c_H . In this case, $n(X, s, \tau)$ is spatially homogeneous and subsequently the tumour comprises only TDCs exposed to normoxia. As a result, the tumour eventually becomes extinct, and $m(\tau)$ decays at a rate which matches d_{TDC} (results not shown), the rate at which TDCs die under normoxia.

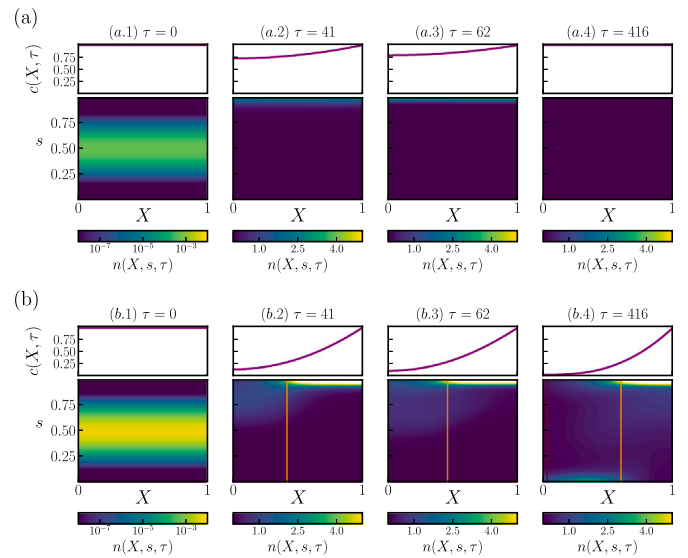


Fig. 7. Series of plots showing how the cell distribution $n(X, s, \tau)$ changes over time for the two cases considered in Fig. 6. We observe long-time extinction when $m_0 = 10^{-4}$ (Fig. 7(a)) and evolution to a persistent tumour cell population when $m_0 = 10^{-3}$ (Fig. 7(b)). Parameter values: as per Fig. 6.

Having understood the mechanism that drives the divergent behaviour observed in Fig. 6, we focus now on the case for which the tumour persists (i.e., $m_0 = 10^{-3}$). Fig. 8 shows how the tumour's phenotypic composition evolves over time. When the hypoxic region first forms, the DCs are localised in the hypoxic niche (see Fig. 8(b)) and the normoxic region contains only TDCs (see Fig. 8(c)). For $41 < \tau < 62$, TDCs in the outer, normoxic region die while DCs in the hypoxic niche survive but do not proliferate. As a result, the tumour's net growth rate is negative. At later times, the DCs diffuse from the hypoxic to the normoxic region where they resume proliferation and drive the observed increase in $m(\tau)$. This creates a feedback loop: as $m(\tau)$ increases, the size of the hypoxic region increases, creating a niche which favours the development of CSCs, which are needed to maintain tumour growth. As shown in Fig. 8(d), CSCs only appear at later times ($\tau \approx 75$) and are localised in hypoxic regions (see $\pi_{CSC}(X, \tau)$ in Fig. 8(a)). At long times, the fraction of CSCs increases and asymptotes to approximately 25% so that $\Pi_{CSC}(\tau) \approx 25\%$ for $\tau \geq 350$ (≈ 50 weeks). The TDCs remain the dominant cell phenotype, with $\Pi_{TDC}(\tau) \approx 50\%$ for $\tau \geq 350$. While CSCs and TDCs localise in distinct tumour regions, DCs eventually spread uniformly across the tissue (Fig. 8(b)). Thus our model predicts coexistence of CSCs, DCs and TDCs within the tumour; CSCs and TDCs are localised in the hypoxic and normoxic niches respectively, while DCs are spread everywhere in the tumour where they coexist with CSCs and/or TDCs.

4. Stationary solutions in the absence of treatment and their local stability

In this section, we use numerical bifurcation analysis (as discussed in Section 2.2) to characterise stationary solutions (i.e., solutions of the form $\bar{n} = \bar{n}(X, s)$ and $\bar{c} = \bar{c}(X)$) of the model in the absence of treatment (Eqs. (5)–(6) and (9)–(11)) and their linear stability. Based on numerical simulations, we find that, on the long time scale, the system converges to stationary profiles (i.e., $\lim_{\tau \rightarrow \infty} n(X, s, \tau) = \bar{n}(X, s)$ and $\lim_{\tau \rightarrow \infty} c(X, \tau) = \bar{c}(X)$). However, we cannot exclude the existence of additional attractors, such as periodic orbits.

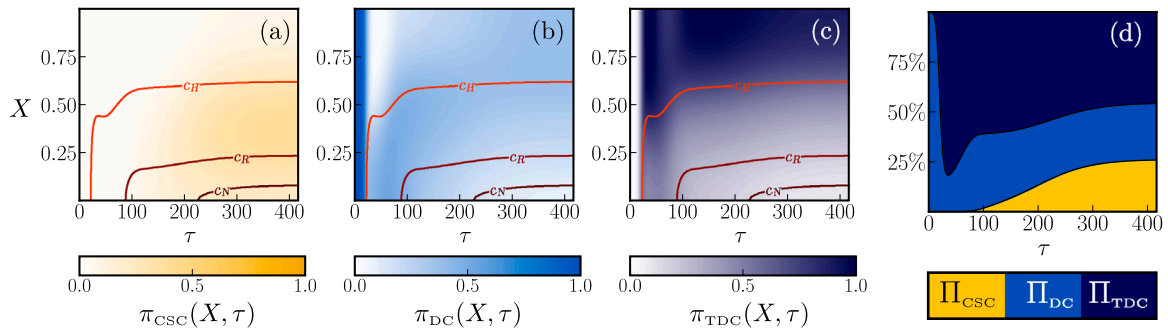


Fig. 8. Series of plots showing how, for the simulation presented in Fig. 7(b), the tumour composition changes over time. All parameters are fixed at the default values stated in Table B.2 with $\gamma_0 = 4.00D_{xc}$ and $m_0 = 0.001$. (a)–(c) Local subpopulation distribution $\pi_i(x, t)$ as defined by Eqs. (14); (d) cumulative plot showing the time evolution of the cell fractions $\Pi_z(t)$, with $z \in \{CSC, DC, TDC\}$, as defined in Eq. (15).

4.1. Spatially-homogeneous stationary solutions

We start by considering spatially-homogeneous stationary solutions (i.e., solutions of the form $\bar{n} = \bar{n}(s)$, $\bar{c} \equiv 1$). The trivial solution $\bar{n} \equiv 0$ and $\bar{c} \equiv 1$, which corresponds to “tumour extinction”, is one such solution that exists for all parameter values. In Appendix C.1, we show analytically that the “tumour extinction” solution is stable if and only if the trivial solution ($\bar{n} = 0$) is a linearly stable stationary solution for the well-mixed formulation of the model, which is obtained setting $D_{xn} = 0$, in Eqs. (5) and assuming a spatially uniform oxygen distribution, with $c \equiv 1$. This is because, when the spatial perturbations are decomposed into Fourier modes, the perturbation with wavenumber $\omega = 0$ (which corresponds to the well-mixed case) is the most unstable wavenumber and, hence, it determines the stability of the trivial steady state. Based on the analytical results in Appendix C.1, we conclude that spatial effects (i.e., the parameters D_{xn} , D_{xc} and γ_0) will not affect the stability of the trivial steady state. In contrast, the stability of the trivial steady state depends on p_{CSC}^{max} , p_{DC}^{max} , d_{TDC} , D_{sn} and V_+ . For example in Fig. 9, we show how the stability of the steady states depends on V_+ and the tumour growth rate. To do so, we write $p_{DC}^{max} = \bar{p}$ and $p_{CSC}^{max} = \delta_p \bar{p}$, where we fix $\delta_p = 0.25$ while we allow \bar{p} to vary. For sufficiently small values of V_+ the trivial solution is unstable (see Fig. 9). However, when V_+ passes through the threshold $V_+^{(cr)}$, a bifurcation occurs that leads to a change of stability. The picture remains qualitatively similar as \bar{p} varies, although for rapidly proliferating cells the bifurcation point $V_+^{(cr)}$ moves to the right.

When $\gamma_0 > 0$ in Eq. (11), the trivial solution is the unique spatially-homogeneous stationary solution. Additional spatially-homogeneous (physical) solutions exist when $\gamma_0 = 0$. We compute such solutions and estimate their stability as we vary V_+ using the numerical techniques described in Section 2.2. Results are summarised in bifurcation diagrams that illustrate how the tumour burden, \bar{m} , of the computed stationary solutions as a function of V_+ . In Figs. 10(a) and 10(b), we show the bifurcation diagrams for a fast-proliferating ($\bar{p} = 0.48$) and a slow-proliferating ($\bar{p} = 0.24$) tumour, respectively. Their qualitative behaviour is similar and the diagram in Fig. 10(b) appears as a translation of Fig. 10(a) along the V_+ axes. For sufficiently small V_+ , the trivial steady state is unstable and a stable non-trivial solution, characterised by a non-zero tumour burden, exists (see upper green branch). As V_+ increases, \bar{m} decreases until V_+ reaches the critical value $V_+^{(cr)}$ (indicated by the yellow dot) where the two solution branches cross and exchange stability via a transcritical bifurcation. For $V_+ > V_+^{(cr)}$, the trivial solution is the unique, physically-realistic steady state solution and it is stable. In the inset of each bifurcation diagram, we illustrate the solution $\bar{n}(s)$ corresponding to a tumour burden of $\bar{m} \approx 0.4$. Again the predictions for fast- and slow-proliferating tumour are similar, with tumours being composed primarily of terminally differentiated cells. More generally, we find that it is possible to map stationary solutions for a rapidly proliferating tumour to that of a slow-proliferating one provided the advection velocity V_+ is decreased. Therefore, in what follows we focus on rapidly proliferating tumours.

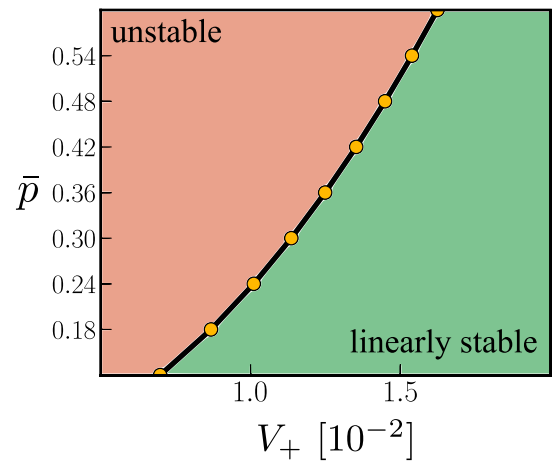


Fig. 9. Plot illustrating how the stability of the trivial steady state changes as the parameters V_+ and p_{DC}^{max} vary. In computing this diagram we assume that $p_{DC}^{max} = \bar{p}$ and $p_{CSC}^{max} = \delta_p \bar{p}$, and we fix $\delta_p = 0.25$ and other parameters as in Table B.2. For discrete values of \bar{p} we numerically estimate the location of the transcritical bifurcation (see yellow dots in the diagram). The black curve that separates the regions of stability and instability that are obtained by interpolating yellow dots.

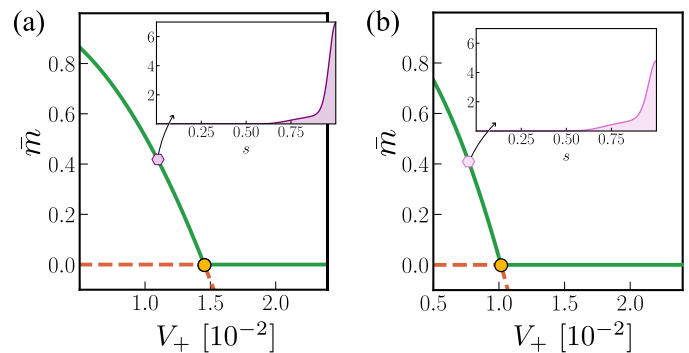


Fig. 10. (a-b) Bifurcation diagrams with respect to V_+ for $\gamma_0 = 0$ and a fast - $\bar{p} = 0.48$ (a) and slow - $\bar{p} = 0.24$ (b) proliferating tumour. Other parameters are as in Table B.2. The insets of each diagram illustrate the solution ($\bar{n} = \bar{n}(s)$) corresponding to the point on the bifurcation diagram marked by a hexagon. Yellow dots indicate transcritical bifurcations.

4.2. Full bifurcation analysis: the emergence of spatially-heterogeneous stationary solutions

Having discussed the spatially-homogeneous stationary solutions of the model, we now present the results of the numerical bifurcation

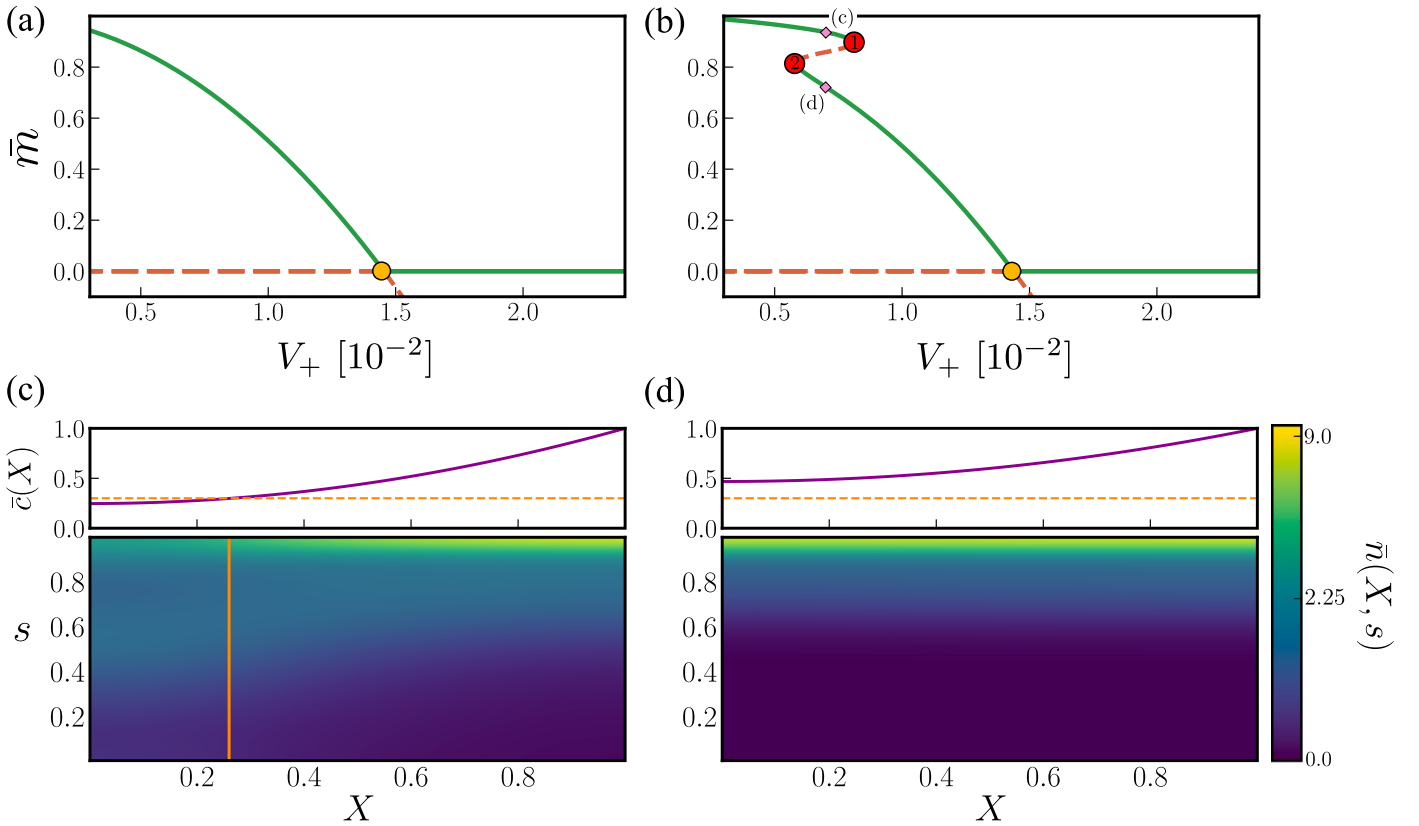


Fig. 11. Series of diagrams showing the bifurcation diagrams of Eqs. (5)–(6) with respect of parameter V_+ for two fixed values of γ_0 : (a) $\gamma_0 = 0.0$ and (b) $\gamma_0 = 1.65D_{xc}$. We distinguish between stable (solid) and unstable (dashed) solution branches and highlight saddle-node and transcritical bifurcations points with red and yellow circles respectively. (c)–(d) Plots of the stable stationary solution corresponding to $V_+ = 0.007$ for $\gamma_0 = 1.65D_{xc}$. The panels (c) and (d) correspond to the upper and lower branch solution respectively. We note that in (d) while the tumour composition is approximately spatially-homogeneous the oxygen concentration $\bar{c}(X)$ is not.

analysis for general stationary solutions $(\bar{n}(X, s), \bar{c}(X))$ of Eqs. (5)–(6) and (9)–(11).

The bifurcation diagrams in Fig. 11 show how the tumour burden of stationary solutions, \bar{m} , changes as V_+ varies for two values of γ_0 . Fig. 11(a) corresponds to $\gamma_0 = 0$ and, as such, it is identical to Fig. 10(a). As γ_0 increases above the critical value $\gamma_0^{(cr)} \approx 1.62D_{xc}$, we observe a significant change in the bifurcation diagram, with new steady state solutions and new bifurcation points emerging. In particular, two saddle-node bifurcation points emerge, SN_1 and SN_2 , which delimit the region of multistability. We note that the structure of the trivial branch remains unaltered when γ_0 varies. This is consistent with the analysis in Appendix C.1. In Fig. 11(b), for small V_+ , there exists a single stable steady state, with a large tumour burden, $\bar{m} > 0.9$. As shown in Fig. 11(c), this solution is spatially heterogeneous both with respect to the oxygen concentration (\bar{c}) and the tumour cell distribution (\bar{n}). In the oxygen-rich region near the vessel (i.e., $X = 1$), the tumour is primarily composed of TDCs. By contrast, the interior of the tumour (i.e., $X \approx 0$) is hypoxic ($c < c_H$) and contains TDCs and a small fraction of CSCs. As V_+ increases, the system undergoes a saddle node bifurcation (SN_2) at which a new type of stationary solution, with a lower tumour burden, emerges. As shown in Fig. 11(d), this solution corresponds to a spatially homogeneous (but phenotypically heterogeneous) tumour even though the oxygen levels, $\bar{c}(X)$, are spatially heterogeneous. This is because, given the lower tumour burden, oxygen levels remain above the hypoxic threshold (c_H). Since tumour cells, regardless of their location, experience high-oxygen levels, they differentiate (see Fig. 2). As a result, TDCs are prevalent everywhere in the tumour. As V_+ increases further, there is a second saddle-node bifurcation (SN_1) at which the spatially heterogeneous solution disappears. Beyond this point a unique, non-trivial, stable steady state exists

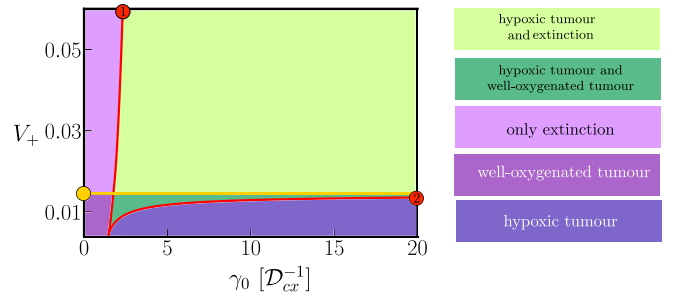


Fig. 12. Continuation of the fold points SN_1 and SN_2 (red curve) and transcritical bifurcation (yellow curve) in the (γ_0, V_+) parameter space for $\bar{p} = 0.48$. Here SN_1 and SN_2 are as identified in the bifurcation diagrams in Figs. 11. The curves associated with the bifurcation points divide the parameter spaces in regions where the model admits a different number/type of (non-negative) stable stationary solutions (as indicated by the different colours). The two saddle-node bifurcations emerge from a cusp point.

which corresponds to a spatially-homogeneous tumour whose mass decreases with V_+ until it crosses the trivial branch when $V_+ = V_+^{(cr)}$ (the yellow circle in Fig. 11(b)). Beyond the transcritical bifurcation, the trivial steady state ($\bar{m} = 0$) is the unique stable solution.

In Fig. 12 we plot the location of the fold points SN_1 and SN_2 as V_+ and γ_0 vary. For sufficiently small γ_0 , there are no fold points (and the bifurcation diagram is analogous to Fig. 11(a)). The two fold points SN_1 and SN_2 emerge from a singular cusp point (located at $(\gamma_0, V_+) \approx (1.523D_{xc}, 0.004)$), and then diverge. While SN_1 initially increases rapidly with γ_0 , reaching large values of V_+ , the trajectory of SN_2 asymptotes to a finite value of the advection velocity, $V_+^{(cr)}$,

as $\gamma_0 \rightarrow \infty$. Here $V_+^{(cr)}$ corresponds to the value of V_+ at which the system has a transcritical bifurcation (see Fig. 11(a)) whose location is independent of the parameter γ_0 . Since SN_2 becomes infinite at a finite value of V_+ , our analysis suggests that the transcritical bifurcation and SN_2 annihilate each other as $\gamma_0 \rightarrow +\infty$. The trajectories of the bifurcation points partition the (γ_0, V_+) -plane into 5 regions corresponding to qualitatively different asymptotic solutions. For small γ_0 , the model admits a unique stable (and non-negative) stationary solution, which is the trivial steady state if $V_+ > V_+^{(cr)}$ and a non-trivial solution, corresponding to a well-oxygenated spatially homogeneous tumour, if $V_+ < V_+^{(cr)}$. As γ_0 increases and crosses the trajectory of SN_1 , the system admits multiple physical solutions. If $V_+ < V_+^{(cr)}$ (i.e., dark green region), the model admits two non-trivial steady states (as illustrated in Fig. 11). On the contrary, if $V_+ > V_+^{(cr)}$ (i.e., light green region), the two stable stationary solutions are tumour extinction and a spatially heterogeneous (hypoxic) tumour. For $V_+ < V_+^{(cr)}$, if γ_0 increases and crosses the trajectory of SN_2 , we enter the dark purple region, where the stationary solution corresponding to a spatially-homogeneous tumour disappears and the model admits only one stable solution corresponding to spatially-heterogeneous tumour. For the range of parameter values considered (which are biologically realistic), we find that the largest region is the light-green one. This is also the region of most interest to us, since it allows for the possibility of driving the tumour to extinction by applying treatment without having to change other model parameters.

As mentioned before, varying \bar{p} (at least in the parameter range considered) does not significantly influence the model's bifurcation structure. When re-computing Fig. 12 with \bar{p} reduced from $\bar{p} = 0.48$ to $\bar{p} = 0.24$, the resulting plot resembles Fig. 12 although the red and yellow curves are vertically translated towards smaller values of V_+ (see Fig. C.21 in Appendix C.1).

5. Characterisation of spatially-heterogeneous tumours

The results from Section 4 pertain the local stability of the different steady states of the system. From a mathematical point of view, it is possible to drive the tumour to extinction, if the trivial solution is locally stable and if the system enters the basin of attraction of the trivial steady state. The question of interest is, therefore, what are the mechanisms responsible for tumour extinction. To answer this question, we have to study the system dynamics. In doing so, we focus on parameter regimes where the model predicts two stable non-negative solutions, one of which is the extinction case (see light green region in Fig. 12). In particular, we consider three representative parameter sets (A, B and C) that can be interpreted as tumours with different characteristics: (A) low oxygen requirement ($\gamma_0 = 2.0D_{xc}$) but fast development ($\bar{p} = 0.48, V_+ = 0.0192$); (B) high oxygen requirement ($\gamma_0 = 4.0D_{xc}$) and fast development ($\bar{p} = 0.48, V_+ = 0.0192$); (C) high oxygen consumption ($\gamma_0 = 4.0D_{xc}$) but slow development ($\bar{p} = 0.24, V_+ = 0.0103$). For each tumour, we first describe their equilibria and then their dynamics in the absence of treatment. In Section 6, we will investigate their response to treatment.

In Figs. 13, we compare the stationary (non-trivial) solutions (see Fig. 13(b)) and corresponding overall statics, such as tumour burden and phenotypic composition (see Fig. 13(a)), for our three representative parameter sets. Comparing tumours A and B, we find that A has a larger tumour burden, \bar{m} ; nonetheless, the two tumours have a similar phenotypic composition (see Fig. 13(a)), with steady state B containing a slightly higher fraction of CSCs. Nonetheless, there is a marked difference in the equilibrium cell densities, $\bar{\phi}(X)$, and oxygen distribution, $\bar{c}(X)$. For steady state B, $\bar{\phi}$ is maximal on the boundary $X \approx 1$ (where the vessel is located) and decreases monotonically towards the interior, where $c < c_N$ (i.e., the necrotic region). This suggests that, while necrosis may decrease the total tumour burden, it does not necessarily impact the overall phenotypic composition of

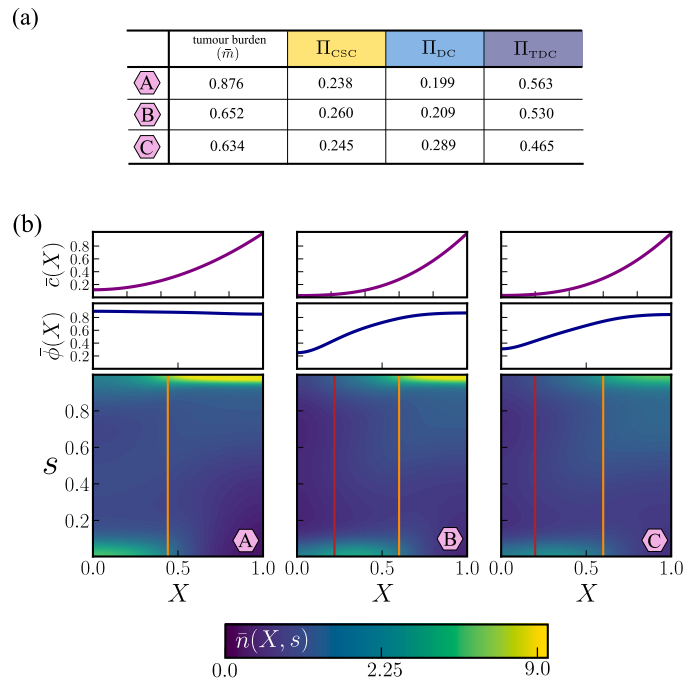


Fig. 13. Characterisation of the non-trivial stationary solutions of Eqs. (5)–(6) for tumours A-C. (a) Table indicating the tumour burden and phenotypic composition (Π_i see Eq. (15)) for the stationary solutions associated with tumours A-C illustrated in panel (b). (b) We illustrate the non-trivial stationary solution, i.e., oxygen profile \bar{c} , rescaled cell number density $\bar{\phi}$, and the local distribution of cell phenotype \bar{n} associated with tumours A, B and C. In the surface plot for \bar{n} , the vertical orange and red lines indicate the boundaries of the hypoxic (X_H where $\bar{c}(X_H) = c_H$) and necrotic regions (X_N where $\bar{c}(X_N) = c_N$), respectively. All parameters are fixed at the default values stated in Table B.2 with (A) $\gamma_0 = 2D_{xc}$, $\bar{p} = 0.48$ and $V_+ = 0.0192$; (B) $\gamma_0 = 4D_{xc}$, $\bar{p} = 0.48$ and $V_+ = 0.0192$; (C) $\gamma_0 = 4D_{xc}$, $\bar{p} = 0.24$ and $V_+ = 0.0103$.

the tumour. Nonetheless, as we show below, tumours A and B have markedly different responses to treatment. Looking now at tumour C, this has a similar tumour burden as tumour B. When comparing the phenotypic composition (Fig. 13(a)), we note an increase in the fraction of DCs in the population in scenario C compared to scenario B. When comparing the local distribution of cell phenotype \bar{n} (Fig. 13(b)), we find this discrepancy is due to a less marked accumulation of TDCs in the oxygenated region near the vessel ($X = 1$) that allows more space for the subpopulation of DCs to expand. This is because in tumours B and C TDCs die at the same rate, d_{TDC} , but the influx of TDCs along the phenotypic axis is smaller for tumour C than B due to the decrease in V_+ . Nonetheless, the difference between the two cases is negligible. This is in line with our previous claim that, at least at equilibrium, a rapidly proliferating tumour behaves similarly to a slowly proliferating one, provided that the advection velocity is decreased.

5.1. Dynamic simulations: switching between basins of attraction

In this section, we investigate how a tumour's initial composition affects its long time behaviour. As before, we impose initial conditions in which the cell distribution is uniform in space and normally distributed along the stemness axis (see Eq. (13)). We fix $\sigma_s^2 = 0.02$ and investigate how the long time behaviour changes as the initial tumour burden m_0 and the mean phenotype s_0 vary. We restrict attention to $s_0 \in [0.25, 0.75]$ so that boundary effects do not distort the Gaussian profile. In Fig. 14, we present results from dynamic simulations. In Figs. 14(a)–14(c) each red curve corresponds to tumour extinction and to a specific cross in the (s_0, m_0) plane in Figs. 14(d)–14(f); the

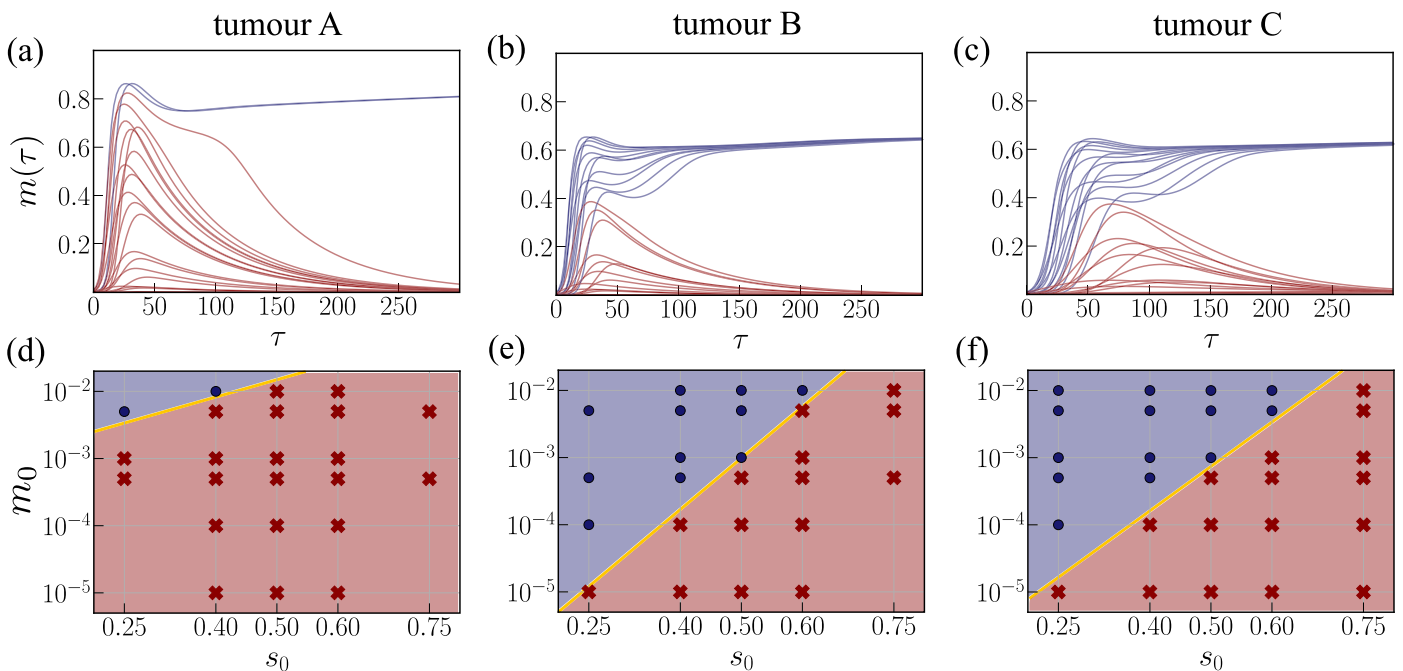


Fig. 14. Series of plots showing how the long time behaviour of a tumour depends on its initial composition. We compare predictions for tumours A (left column), B (middle column) and C (right column) as defined in Section 5. We plot the evolution of the tumour burden as predicted by Eqs. (5) and (8)–(11) for the initial condition (13) (see first row). Each curve in Figs. 14(a)–14(c) corresponds to a point in the (m_0, s_0) diagram in Figs. 14(d)–14(f); red crosses indicate initial conditions that result in tumour extinction, blue dots indicate instead tumour invasion. We use the estimated point to approximate the regions of the (m_0, s_0) space that map to extinction (red region) and tumour invasion (blue region). We approximate the boundary by the yellow curve $m_0 = m_{cr}(s_0)$. All parameters are fixed at the default values stated in Table B.2 with (A) $\gamma_0 = 2D_{xc}$, $\bar{p} = 0.48$ and $V_+ = 0.0192$; (B) $\gamma_0 = 4D_{xc}$, $\bar{p} = 0.48$ and $V_+ = 0.0192$; (C) $\gamma_0 = 4D_{xc}$, $\bar{p} = 0.24$ and $V_+ = 0.0103$.

blue curves correspond to “tumour-invasion” and are indicated by blue circles in Figs. 14(d)–14(f). For tumour A, which is characterised by a small oxygen consumption rates (see Figs. 14(a) and 14(d)), most initial conditions considered yield to tumour extinction. In contrast, for tumours B and C, extinction is less likely. Figs. 14(a)–14(c) show that the tumour burden $m(\tau)$ does not decay monotonically; rather, it grows initially, to relatively large values ($m \approx 0.75$) in some cases, and only starts to decay at longer times. While tumour A can attain a tumour burden as large as $m = 0.8$ and still decay to extinction, tumours B and C successfully invade the tissue once they pass the much lower threshold $m = 0.4$. Comparing Figs. 14(b) and 14(c), we find that tumours B and C exhibit a similar growth dynamics except that tumour B evolves more rapidly (as expected since it consists of cells with a larger proliferation rate).

Based on the numerical simulations, we decompose the (s_0, m_0) plane into two distinct regions: one that maps to tumour-invasion (blue) and one that maps to tumour-extinction (red). The boundary between these regions can be approximated by the function $m_0 = m_{cr}(s_0)$. Accordingly, for any mean phenotype s_0 , all tumours with initial mass $m_0 > m_{cr}(s_0)$ will persist. Interestingly, the model predicts that m_{cr} increases with s_0 , suggesting that as the proportion of stem-like cells ($s_0 \ll 1$) initially present increases, the smaller the value of m_0 for which invasion occurs. On the other hand, as $s_0 \rightarrow 1$, even large tumours may be eliminated. In this case, the tumour initially comprises TDCs which are unable to drive tumour growth. This is consistent with the idea that CSCs have the unique capacity to drive the formation and maintenance of tumours. This effect is more pronounced for tumours with larger consumption rate, with tumour survival occurring across a wider range of values of s_0 and m_0 when the consumption rate is increased from $\gamma_0 = 2.0D_{xc}$ (Fig. 14(a)) to $\gamma_0 = 4.0D_{xc}$ (Figs. 14(b) and 14(c)). On the contrary, we find the likelihood of tumour survival is approximately the same when fixing γ_0 and changing the growth dynamics from fast (Fig. 14(b)) to slow (Fig. 14(c)).

When applying treatment, the aim is to drive the tumour into the extinction region. Therefore, we expect that it will be easier to

eradicate tumours with a larger extinction region. From this point of view, comparing Figs. 14(d)–14(f), we see that the size of the extinction region decreases as the oxygen consumption rate increases, suggesting that tumours with higher oxygen consumption rates (*i.e.*, B and C) are more resilient, even though they have a lower tumour burden (see Fig. 13(a)). This is because, as the rate at which cells consume oxygen increases, hypoxic regions are initiated at smaller tumour volumes (*i.e.*, smaller numbers of tumour cells), creating an environment in which CSCs can emerge and sustain tumour growth (as in Fig. 13(a), tumours B and C).

6. Dynamics in the presence of treatment

Having used our model to study tumour growth in the absence of treatment, we now use it to investigate tumour responses to radiotherapy, focusing on characterising the impact of phenotypic and spatial heterogeneity on treatment outcomes. Due to the large number of unknown parameters, it is difficult to apply our model to patient specific data and personalised radiation scheduling. However, we believe that the model can provide insight into the ways in which interactions between the different radio-resistance mechanisms determine treatment responses and, in doing so, increase understanding of the possible causes of relapse.

We parametrise the survival fraction, Eq. (12a), with parameter estimates from the literature on prostate cancer. As in Section 5.1, we compare the responses of our three tumours (A, B and C) with the aim of capturing some of the inter-patient heterogeneity. We recall for tumours A–C extinction is possible. For each tumour, we consider as initial conditions the corresponding non-trivial (spatially-heterogeneous) equilibrium solutions (*i.e.*, steady states A, B and C in Fig. 13). Standard of care regimens correspond to 2.0 Gy/fraction given 5 days/week. More recently, due to the improvements in the precision of RT, hypofractionated RT (HFRT) has been proposed as an alternative to standard of care for several types of cancer, including prostate cancer (Dearnaley et al., 2016) where larger doses of RT are given over a shorter

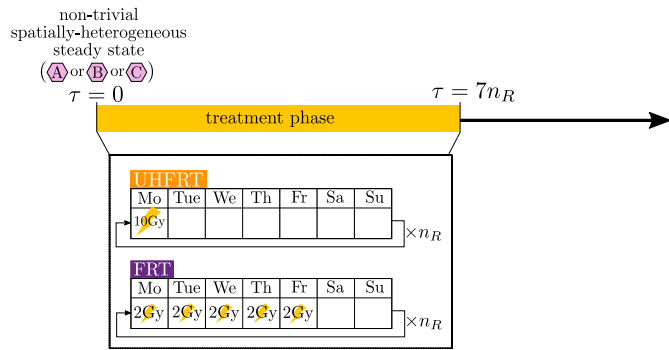


Fig. 15. Schematic diagram showing how treatment is incorporated into the model. Treatment is repeated over a period of n_R weeks so that the final dosage delivered is $10 \times n_R$ Gy. We consider two different protocols: ultra-hypo-fractionated radiotherapy (UHFRT), and fractionated radiotherapy (FRT). For UHFRT, a single dose of 10 Gy is delivered on Monday of each week during treatment; for FRT, 5 doses of 2 Gy are delivered on Monday to Friday, with a break from treatment on Saturday and Sunday.

period of than standard RT. Hypofractionation is commonly subdivided into “moderate hypofractionation” (2.4–3.4Gy per fraction) and “ultra-hypofractionation” (5Gy or more per fraction). In Section 6.1, we investigate how different fractionation strategies impact the evolution of the phenotypic composition of the tumour during treatment. To this end, we consider two different fractionation strategies. As shown in Fig. 15, we assume that tumours receive 10 Gy of radiotherapy every week for n_R weeks. Treatment is delivered either as a single, high dose (Mo) or as 5 doses (Mo-Fr) with a two-day break (Sa-Su). We refer to the first treatment strategy as ultra-hypofractionated radiotherapy (UHFRT) and the second one, which corresponds to standard-of-care, as fractionated radiotherapy (FRT).

In terms of RT scheduling, optimisation considers the total number of doses and the level of fractionation as described by the *Biologically Effective Dose* (BED) (Barendsen, 1982; Fowler, 1989). The BED provides a measure of the total biological dose of RT delivered to a tissue during a treatment protocol, based solely on changes in tumour burden during treatment. Under the assumption that α and β in the LQ model (12a) are constant parameters, the BED for a treatment consisting of z fractions of d Grays is defined as $BED_{d \times z} = zd(1 + d/(\alpha/\beta))$ (Jones et al., 2001). For example, considering tumour B at equilibrium (Fig. 13(b)), we find that $\bar{\alpha}_T/\bar{\beta}_T \approx 7.8$, where the subscript T indicates values averaged over the whole tumour (e.g., $\bar{\alpha}_T \equiv \bar{\phi}^{-1} \int_0^1 \int_0^1 \alpha \bar{n}(X, s) dX ds$). Similar results are obtained for tumours A and C for which we find that $\bar{\alpha}_T/\bar{\beta}_T \approx 7.4$ and $\bar{\alpha}_T/\bar{\beta}_T \approx 7.8$. Therefore, we might expect the three tumours to have similar responses to RT. However, in our model, α and β (for the overall tumour) are not constant and may change during treatment, as this affects the tumour’s internal composition and its micro-environment (i.e., oxygen levels). Consequently, we expect other factors besides fractionation, such as the time at which a dose is administered, to impact the overall outcome and these must, therefore, be taken into consideration when planning treatment schedules. In Section 6.2, we instead investigate the impact that RT schedules have on treatment outcomes and show that cell-killing alone is not always a good predictor of treatment efficacy.

6.1. Numerical simulations

In Fig. 16, we show the evolution of the tumour burden $m(\tau)$ during, and after, exposure to the two treatment protocols in Fig. 15 for 5 weeks (total of 50 Gy). Each panel corresponds to a different tumour. Taking tumour B as a reference, we recall that tumour A is obtained by decreasing the oxygen consumption rate (lower γ_0), while tumour C is obtained by decreasing the proliferation and differentiation rates (lower \bar{p} and V_+). Using this reference value of $\bar{\alpha}_T/\bar{\beta}_T$ for all three

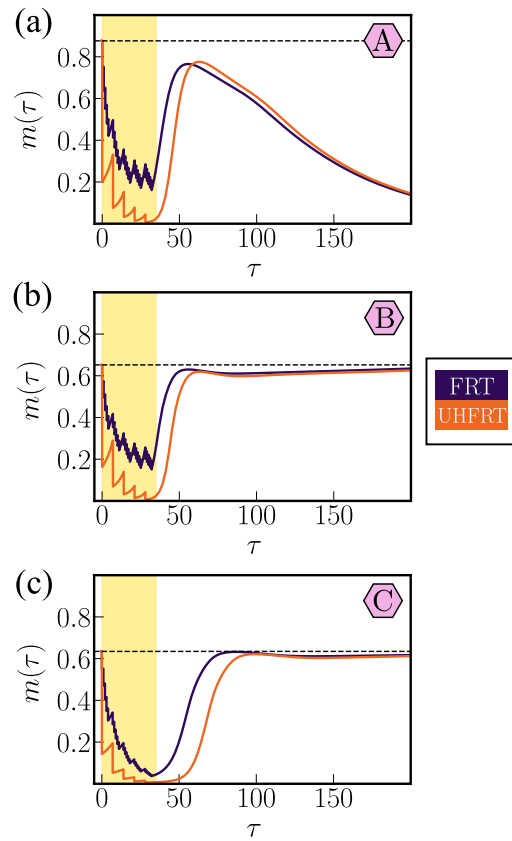


Fig. 16. Evolution of the tumour burden, $m(\tau)$, during treatment for the three different parameter sets: A, B and C as in Fig. 13. We compute $m(\tau)$ numerically by solving Eqs. (5) and (8)–(12), starting from the corresponding non-trivial steady state (see Fig. 13(b)), and applying 50 Gy radiotherapy over a period of 5 weeks according to the two protocols described in Fig. 15. The duration of treatment is highlighted by the yellow area. The remaining parameters are fixed at the default values listed in Tables B.1–B.2.

tumours, we estimate that the BED of the UHFRT protocols, $BED_{10 \times 5}$, is almost twice the BED for the FRT protocols, $BED_{2 \times 25}$ (for example, for tumour B we find $BED_{2 \times 25} = 62.82$ and $BED_{10 \times 5} = 114.1$). This suggests that, for any given tumour, the UHFRT is more effective in reducing tumour burden than the FRT protocols. However, we find that the biological response of the tissue as measured by the reduction in tumour burden cannot explain treatment outcomes. For tumour A, a 5-week course of treatment is sufficient to eradicate the tumour, regardless of the protocol used (see Fig. 16(a)). By contrast, Figs. 16(b) and 16(c) show that the tumours with higher γ_0 recur, regardless of the protocol chosen: while the tumours initially respond to treatment, they eventually regrow to their original size. When comparing the tumour burdens at the end of treatment for tumours A and B, for FRT and UHFRT, we find that they are similar. Nonetheless the treatment response of the two tumours is markedly different. Comparing instead tumours B and C, for FRT and UHFRT, the tumour burden at the end of treatment is significantly smaller for tumour C (as expected, due to the different growth rates of the two tumours) but recurrence is observed in both cases.

We now consider how the internal phenotypic composition of the tumours changes during treatment, in order to determine whether there is any early indication of different treatment outcomes. We also plot the minimum oxygen concentration recorded in the tissue $\varrho(t) = \min_{X \in [0,1]}(X, \tau)$. The results presented in Figs. 17(a)–17(c) suggest that during UHFRT the tumour composition is independent of γ_0 (compare panels a and b) but it varies significantly with the rate of proliferation/differentiation (compare panels b and c). In all cases, RT

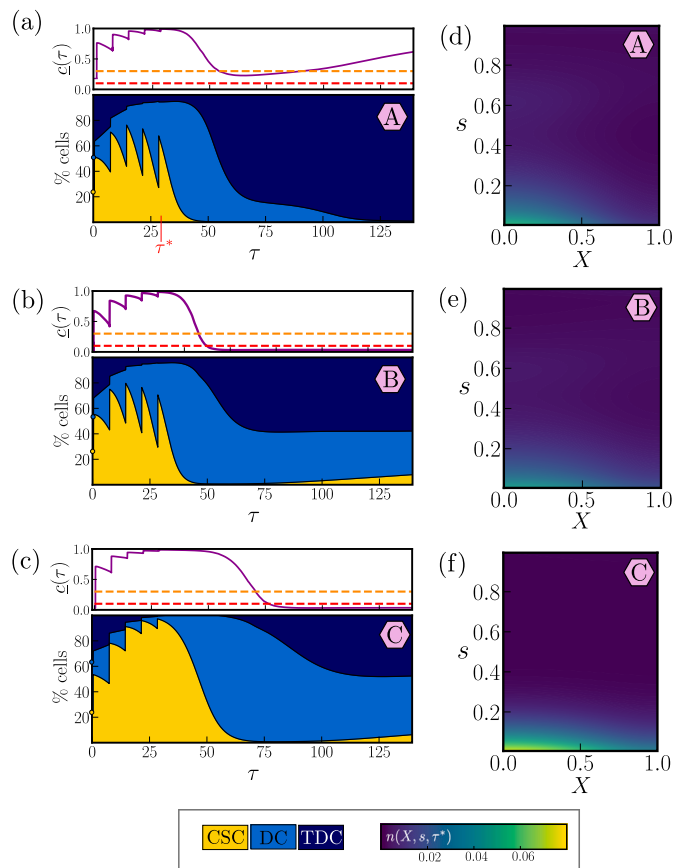


Fig. 17. Numerical results showing how, for the simulations presented in Fig. 16, the tumour’s internal composition changes following 5 weeks of UHFRT for (a) and (d) tumour A, (b) and (e) tumour B and (c) and (f) tumour C. The top panels in (a)–(c) illustrate the evolution of the minimum oxygen level within the tumour, $\underline{c}(\tau) = \min_{X \in [0,1]} c(X, \tau)$. The latter is compared to the oxygen thresholds c_H (orange horizontal line) and c_R (red horizontal line). In the lower panels (d)–(e), we illustrate the cell distribution $n(X, s, \tau^*)$ at the time $\tau^* = 28.5$ shortly after the last dose is administered ($\tau = 28$).

re-oxygenates the tumour ($\underline{c} > c_H$ throughout treatment). Therefore, although $\Pi_{CSC}(\tau)$ increases after each dose of radiotherapy (since RT selects for radio-resistant CSCs), $\Pi_{CSC}(\tau)$ decreases between doses as CSCs tend to differentiate when exposed to sufficiently high oxygen levels. Nonetheless, at 28 days (*i.e.*, just after the last dose), we observe an increase in Π_{CSC} compared to the pre-treatment value. This is more relevant for tumour C where more than 90% of cells are stem-like at the end of treatment. This is due to slower differentiation rate of tumour C and the selection pressure of RT which favours survival of CSCs. By contrast, the fraction of differentiated (highly-proliferative) cells, Π_{DC} , decreases significantly after each dose due to the higher sensitivity of differentiated cells. Inspection of the distribution of cells $n(X, s, \tau)$ at the end of treatment ($\tau = \tau^*$) reveals that RT decreases intra-tumour heterogeneity in both space and phenotype due to the combined effects of re-oxygenation and the selection of resistant phenotypes (see Figs. 17(d)–17(f)). Once treatment halts, CSCs differentiate, replenishing the pool of differentiated cells which drive the rapid regrowth of tumours A and B, and the slower recovery of tumour C. Once the tumour burden increases, tissue oxygen levels decrease. While in tumour A (small γ_0), oxygen levels remain mildly hypoxic ($\underline{c} \approx c_H$), in tumours B and C regions of severe hypoxia eventually develop in which DCs de-differentiate, producing CSCs which enable the tumour to survive and continue to grow.

For FRT (see Figs. 18), the evolution of \underline{c} differs during the early stages of treatment for tumours A, B and C. For tumours A and C,

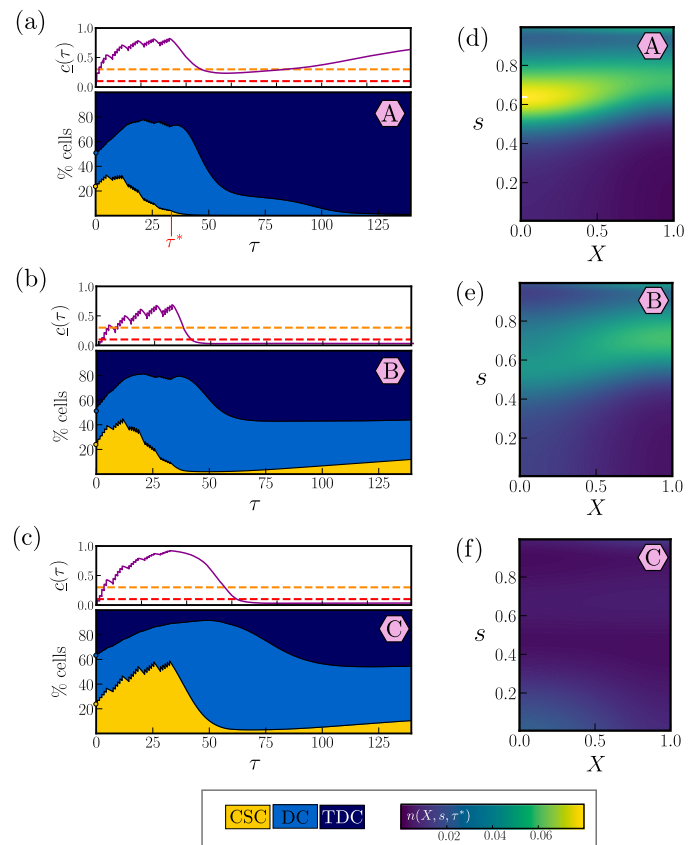


Fig. 18. Numerical results showing how, for the simulations presented in Fig. 16, the tumour’s internal composition changes following 5 weeks of FRT when (a) and (d) tumour A, (b) and (e) tumour B and (c) and (f) tumour C. In the top panels we plot the minimum oxygen level \underline{c} recorded in the tissue at any time and compare it with the relevant oxygen threshold c_H and c_R . In the lower panels (d)–(e), we illustrate the cell distribution $n(X, s, \tau^*)$ at the time $\tau^* = 32.5$ shortly after the last dose is administered ($\tau = 28$).

one cycle of FRT is sufficient to raise oxygen levels above the hypoxic threshold c_H , while for tumour B two cycles are required. The internal composition of the three tumours also differs. In tumours A and B, the fraction of CSCs, $\Pi_{CSC}(\tau)$, at the end of treatment ($\tau = \tau^*$), is much smaller than its initial value. Nonetheless, at all times, a larger fraction of CSCs is present in tumour B due to the delayed re-oxygenation of tumour B compared to tumour A. For tumour C, Π_{CSC} increases overall during treatment it is still significantly smaller than the value recorded after the last dose for UHFRT (see Fig. 17). Overall, FRT is less effective than UHFRT in re-oxygenating the tumour because fewer cells are killed. For tumours B and C, this leads to the formation of an hypoxic region shortly after the end of FRT treatment so that a small fraction of CSCs persists in the tumour at all times, in contrast to the behaviour depicted in Figs. 17(b)–17(c).

On the one hand, the simulation results presented in this section highlight the key role played by the oxygen distribution in shaping a tumour’s response to RT due, in large part, to its (eventual) impact on the dynamics of CSCs. Hence, the dimensionless oxygen consumption rate γ_0 , which influences the distribution of oxygen in the tumour, distinguishes treatment outcomes. Tumours with smaller γ_0 respond better to UHFRT and FRT than those with larger oxygen consumption rates. These findings illustrate the potential therapeutic benefit of combining RT with metabolic inhibitors that reduce oxygen consumption rates in tumour cells by inhibiting mitochondrial activity, and support recent proposals by several experimental studies (Ashton et al., 2016; Fiorillo et al., 2016; Mudassar et al., 2020). On the contrary, we find that the internal composition of the tumour at the end of treatment is markedly

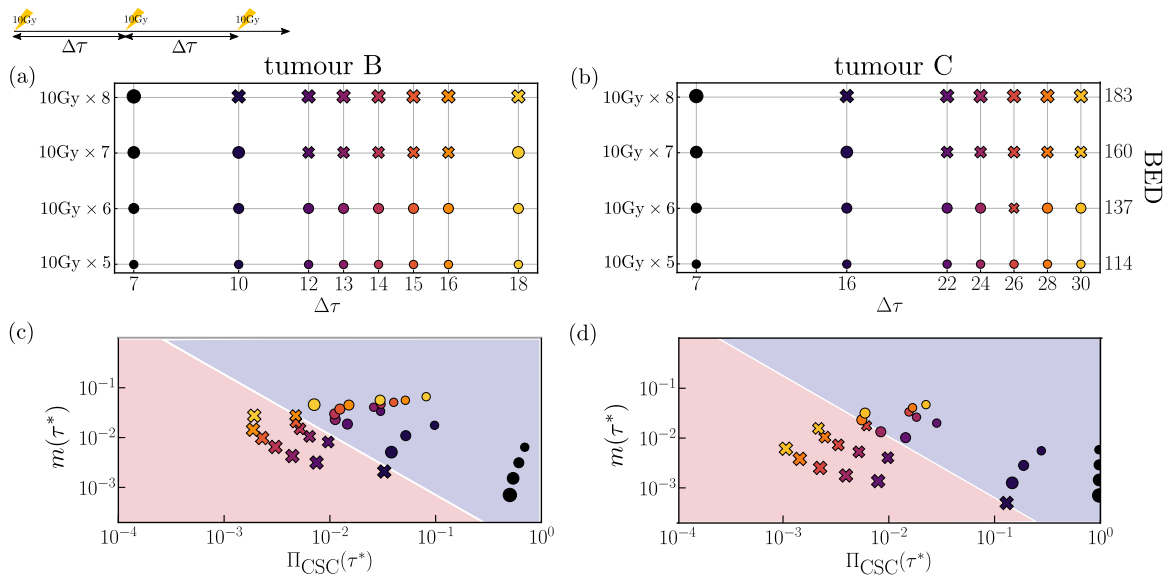


Fig. 19. Comparison of different schedules for UHFRT where the interval between successive doses ($\Delta\tau$, see top schematic) and the total dose given are changed. (a)–(b) Summary of the effect of different treatments (cross: tumour goes extinct; circle: tumour persists) for tumours B (a) and C (b); the size of the crosses/circles increase with the number of doses given while the colour relates to the interval between doses. For each treatment strategy simulated in Figs. 19(a) and 19(b), in Figs. 19(c)–19(d) we illustrate the tumour burden, m , and the fraction of CSCs, Π_{CSC} , at time τ^* right after the last dose is administered ($\tau^* = \tau_f + \epsilon$ where τ_f is the time the last dose is delivered and $\epsilon = 0.0625$). For the markers shape, size and colour, we use the same scheme in Figs. 19(a) and 19(c) and in Figs. 19(b) and 19(d).

influenced by the tumour’s growth dynamics (*i.e.*, the values of \bar{p} and V_+). In particular, we find that selection of radio-resistant CSCs during treatment is more pronounced in tumours that proliferate slowly than those that proliferate rapidly.

6.2. Alternative protocols: the possible benefit of waiting

The results presented above suggest that tumours with higher oxygen consumption rates are more aggressive and may be less responsive to standard treatment. Here we investigate how adapting RT scheduling might improve treatment efficacy. This is motivated by the observation that the overall tumour sensitivity may change during treatment, as treatment affects the tumour’s phenotypic composition and its micro-environment (*i.e.*, oxygen levels). Specifically, we use our model to test whether waiting longer periods between treatment cycles (for example, we might repeat treatment every two weeks instead of every week) can be beneficial. In doing so, we focus on the more aggressive tumours B and C. We again deliver treatment in rounds of 10 Gy either in smaller doses of 2 Gy for 5 consecutive days (FRT) or in one single dose (UHFRT), but we consider different waiting times between consecutive rounds of treatment. In practice, when assessing RT treatments, clinicians should ensure that the maximum tolerable dose (*i.e.*, the highest dose of a treatment that does not cause unacceptable side effects (Gad, 2014)) is not exceeded. To this end, there might be limits in how large the total BED can be, in particular when doses larger than 10 Gy are considered due to adverse side effects these may cause (Kainuma et al., 2019).

In Fig. 19, we consider the response of tumours B and C to different UHFRT protocols. Here the interval between cycles of treatment ($\Delta\tau$) corresponds to the interval between consecutive doses (see top schematic in the figure). When the interval between doses is 7 days, as in Fig. 16, treatment fails for both tumours, even when we increase the total dose to 80 Gy. As shown in Fig. 19(c) (see black dots), while treatment successfully reduces the overall tumour burden, it selects for CSCs-like cells that eventually drive tumour recurrence. Increasing the time between doses leads to better treatment outcomes. For example, for tumour B (see first column in Fig. 19), a total dose of 70 Gy is sufficient to prevent recurrence when $\Delta\tau \in (12, 16)$. However, waiting too long (*i.e.*, $\Delta\tau \geq 18$) can be disadvantageous as a larger total dose

is required to drive the tumour to extinction. Fig. 19(c) shows that, in general, the shorter the interval between doses, the smaller the tumour burden at the end of treatment. Yet, recurrence is observed for inter-dose intervals of 7 days and not for intervals of 12 weeks (the latter is true for 70 and 80 Gy total doses). This is because different outcomes cannot be (solely) understood on the basis of the overall tumour burden. Rather, as shown in Fig. 19(c), it is the combined information about tumour burden and the fraction of CSCs’ in the tissue that enables us to predict treatment outcome (this is consistent with the analysis in Section 5.1). Interestingly, we find that $\Pi_{CSC}(\tau^*)$ is not a monotonic function of τ . If the time between doses is too long (*e.g.*, $\Delta\tau = 18$ days for tumour B), tumour regrowth between doses leads to the formation of an hypoxia niche in which CSCs accumulate. The non-monotonic relation between outcome and scheduling hints at the existence of optimal strategies and the possibility of applying optimal control theory to identify such optimal strategies, a topic of practical further interest. A similar trend is predicted for the treatment response of tumour C (see Figs. 19(b) and 19(d)). However, since tumour C grows and differentiates more slowly than tumour B, longer breaks between consecutive RT doses (about 26 days) are needed to improve treatment outcomes: larger values of $\Delta\tau$ are needed to overcome the high selection pressure of RT in favour of CSCs. For example, when exposing tumours B and C to the same 10Gy \times 7 protocol with $\Delta\tau = 16$, we find that tumour B has a much larger tumour burden than tumour C (almost an order of magnitude larger), yet the former goes extinct while the latter does not. This is explained by the different compositions of the two tumours at the end of treatment, in particular the difference in the proportion of CSCs.

When considering FRT, the interval between cycles, $\Delta\tau$, corresponds to the time between the administration of the first of the five 2 Gy doses, which are still delivered over 5 consecutive days (see schematic in Fig. 20). In this case, our model predicts that, for FRT, much shorter inter-treatment cycle intervals are more effective than for UHFRT. As shown in Fig. 20(a), for tumour B, the FRT treatment is most effective when the inter-cycle interval is close to standard of care (7–9 days). Treatment fails for larger intervals ($\Delta\tau \geq 12$) that were instead beneficial when scheduling UHFRT (see Fig. 19(a)). Fig. 20(b) shows that simulations with $\Delta\tau = 13$ accumulate in the top-right corner of the diagram regardless of the BED. This suggests that the tumour

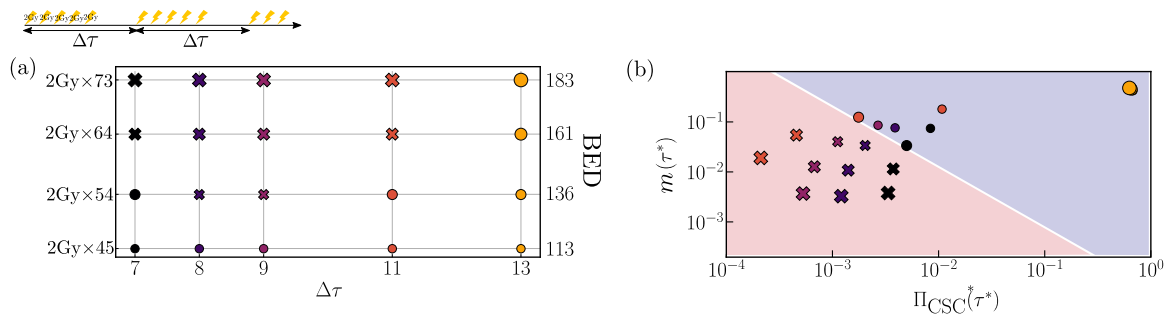


Fig. 20. Comparison of different schedules for FRT where the interval between the first (of the 5) 2 Gy doses delivered for repeats of treatment ($\Delta\tau$, see top schematic) and the total dose given are changed. (a) Summary of the effect of different treatments (cross: tumour goes extinct; circle: tumour persists) for tumour B; the size of the crosses/circles increase with the number of doses given while the colour relates to the interval between doses. For each treatment strategy simulated in Fig. 20(a), in Fig. 20(b) we illustrate the tumour burden, m , and the fraction of CSCs, Π_{CSC} , at time τ^* right after the last dose is administered ($\tau^* = \tau_f + \epsilon$ where τ_f is the time the last dose is delivered and). For the markers shape, size and colour, we use the same scheme in Figs. 20(a) and 20(b). Note that the number of doses delivered are chosen so as to have the same overall BED as in Figs. 19(a)–19(b).

recurs and that treatment favours the accumulation of CSCs in the tissue (see the large value of $\Pi_{\text{CSC}}(\tau^*)$ which exceeds the value at the beginning of treatment). This is because, for large $\Delta\tau$, treatment fails to re-oxygenate the tissue (results not shown). The presence of an hypoxic niche combined with the selective pressure of RT combined drive the accumulation of CSCs, resulting in the overall tumour becoming resistant to treatment. Once treatment ends, the large number of CSCs in the tumour enables it to quickly evolve to a non-zero steady state. When considering, instead, slowly proliferating tumours (results not shown), we find that the response is optimal for $\Delta\tau \approx 16$, an interval which is still much shorter than the optimal value estimated for the UHFRT protocols. This is unsurprising, since we observed that standard of care selects for CSCs in tumour C (see Fig. 18(c)) (hence the advantage in waiting) while it almost eliminates CSCs in tumour B (see Fig. 18(b)).

In summary, our model suggests that optimal schedules for UHFRT and FRT may differ markedly due to the different ways in which the composition of the tumours evolves during the two fractionation protocols. In general, if the RT doses are too close to each other, treatment selects for CSCs which drive disease relapse. If, instead, the RT doses are too far apart, then the tumour has time to regrow between rounds of treatment, and to form a severely hypoxic region, which reduces the overall treatment efficacy and contributes to treatment failure. By choosing an intermediate interval between doses, the model predicts successful extinction of the tumour for physically realistic protocols (with BED in the range 130–160Gy). In this case, successful eradication is due to tumour re-oxygenation and the conversion of potential CSCs into radio-sensitive DCs. Overall, FRT does not lead to accumulation of CSCs during treatment but it is less effective at re-oxygenating the tumour than UHFRT. Consequently, shorter intervals between treatment cycles are predicted to be more effective for FRT protocols than UHFRT. Furthermore, our model predicts that the tumour benefits from different dose schedules and that slowly growing tumours benefit from longer periods of “treatment holidays”.

7. Conclusion

We have proposed and analysed a new mathematical model, structured by phenotype and space, to describe the evolution of intra-tumour heterogeneity in the presence and absence of radiotherapy. We have focused on the role played by tissue oxygen levels in shaping the tumour’s internal phenotypic composition, with hypoxia (*i.e.*, abnormally low oxygen levels) being a key driver of cell de-differentiation towards an aggressive, stem-like phenotype. The limited susceptibility of the CSCs to treatment with radiotherapy is found to play a role in tumours’ relapse.

After introducing our model, in Sections 3–5 we analysed its long time behaviour in the absence of treatment, combining analytical and

numerical techniques to investigate its bifurcation structure as two model parameters vary: the magnitude of the differentiation velocity V_+ and the dimensionless oxygen (and, by extension, nutrient) consumption rate γ_0 . For biologically realistic values of these parameters the system possesses two non-negative steady states which we term “tumour-extinction” and “tumour-invasion”. Based on extensive numerical simulations, we concluded that tumours with relatively large values of γ_0 are more likely to successfully invade the tissue, while tumours with lower oxygen consumption rates γ_0 may be eliminated. This result can be better understood by focusing on a tumour’s internal composition and establishing whether large hypoxic regions appear in its interior. Hypoxic niches are essential for the accumulation and maintenance of cancer stem cells, which, due to their high clonogenic potential, are responsible for the growth and successful invasion of the tumour.

In Section 6, we used the model to study tumour responses to radiotherapy (RT). A key insight from the model is the importance of monitoring a tumour’s burden and its phenotypic composition to predict treatment outcome. In particular, a successful treatment strategy has to jointly control tumour burden and the prevalence of CSCs. Based on this general principle, we then analysed the efficacy of different RT strategies (fractionation and scheduling) on tumours with different properties (that might explain patient-specific outcomes). Here we summarise those of our key findings that could be tested *in vitro* using multi-cellular tumour spheroids:

1. The choice of fractionation protocols impacts the internal composition of the tumour at the end of treatment. While large doses administered less often (10 Gy, 1 day per week) can be more effective in reducing tumour burden they select for radio-resistant CSCs. On the contrary, standard of care fractionation (2 Gy for 5 days per week) prevents the accumulation of CSCs but is less effective in reducing tumour burden. Based on these observations, we conclude that the failure/success of these strategies are associated with different biological mechanisms.
2. Different scheduling of the same fractionation protocol can impact treatment outcome. The results presented in Section 6.2 highlight that, in certain cases, “sooner” is not always “better”. This applies to RT protocols that select for radio-resistant phenotypes (*e.g.*, 10 Gy, 1 day per week). In this case, if the interval between doses is too short, resistant cells accumulate until, eventually, the tumour stops responding to treatment. Longer intervals between RT doses allow CSCs to differentiate (upon RT-mediated re-oxygenation of the tissue) and concentrate cells around a radio-sensitive, differentiated phenotype prior to the next round of treatment, leading to a better overall response. This is analogous to the idea of “treatment holiday” as an optimal

strategy to prevent the emergence of resistance (Pouchol et al., 2018). However, waiting too long between successive doses can be harmful, as the tumour has the time to increase in size and develop extensive hypoxic regions in which radio-resistant CSCs accumulate and all tumour cells are less radio-sensitive due to the lack of oxygen.

3. RT outcomes depend on tumour properties. We find that large values of γ_0 correlate with more aggressive tumours whose elimination requires higher total RT-doses. This is not because of significant differences in tumour composition/burden at the end of treatment but rather because a tumour with higher γ_0 is more likely to invade a tissue, as shown in Section 5.1. On the contrary, differences in the rate of tumour growth (V_+ , \bar{p}) impact a tumour's composition at the end of treatment, with slowly growing tumours being correlated with higher selection of RT-resistant CSCs and smaller tumour burdens. From this point of view, we find that slowly growing tumours may benefit from longer intervals between successive treatment rounds.

7.1. Future directions

It is natural to ask whether our conclusions generalise to more realistic, higher-dimensional spatial geometries, e.g., the framework of tumour spheroids (Bull et al., 2020). When symmetry arguments are used to reduce 3D-problems to 1D geometries, we find that the qualitative behaviour of the model solutions are similar to those reported for the 1D-Cartesian geometry investigated here (results not shown). However, fully 2D and 3D simulations may exhibit additional behaviours not captured by the simplified 1D-geometry. As a first attempt to investigate how heterogeneity impacts tumour evolution and response to treatment, we adopted a simple approach for modelling tumour growth, which is based on reaction–diffusion equations. Alternatively, a more physically-realistic model could be developed using a multiphase framework (Byrne and Preziosi, 2003; Frieboes et al., 2010; Hubbard and Byrne, 2013; Lewin et al., 2020a). Within this approach, a tissue is decomposed into distinct phases (e.g., tumour cells, blood vessels, extracellular fluid). Mass and momentum balances are applied to each phase and the system is closed by making constitutive assumptions about their properties. The resulting models typically comprise mixed systems of PDEs, with physically motivated, non-linear diffusion terms. As our model predicts that oxygen levels play a critical role in tumour development, it would be interesting to investigate how our results generalise when vascular remodelling and angiogenesis are incorporated. Alternatively, a hybrid-modelling framework could be used to study vascular tumour growth (Anderson and Chaplain, 1998; Phillips et al., 2020; Vavourakis et al., 2017).

Our results suggest the possible benefit of combining RT with metabolic inhibitors, as recently proposed by several studies (Ashton et al., 2016; Fiorillo et al., 2016; Mudassar et al., 2020), and/or differentiation therapy (De Thé, 2017) to improve response to treatment. By decreasing the rate at which the cells consume oxygen, oxygen levels in the tumour can be increased to prevent the formation of regions of radio-biological hypoxia and increase the tumour's overall sensitivity to radiotherapy. Furthermore, our model suggests that metabolic inhibitors can also prevent the emergence of CSCs, by re-oxygenation of large hypoxic niches in which stem-like cells initially might accumulate. Differentiation therapy would, instead, induce the loss of CSCs and, thereby, prevent the emergence of resistance. From this point of view, it would be interesting in future work to extend our model to include metabolic inhibitors/differentiation therapy and investigate how they should be combined with RT to improve treatment outcomes. Furthermore, control theory could be used to identify optimal treatment strategies upon definition of a biologically relevant cost function. However, in order to translate the model into the clinic, other important aspects must be considered, including maximum tolerable dose and potential side effects. First, a more detailed model of the

effects of RT on tumour cells should be explored. Here, we assume RT results in instantaneous cell-killing; in practise, however, RT might cause tumour cells to become senescent permanently impairing their clonogenic capacity instead of cell death (Sia et al., 2020). Analogously to TDCs in our model, RT-induced senescent cells might not proliferate but they would still influence the tumour dynamics by consuming oxygen and competing for space. While the standard LQ-model has been widely used in the literature, more recent works have considered more detailed models of RT, either directly incorporating senescence (Brüningk et al., 2018) or including memory effects, with time-delays in cell-killing and cell-proliferation in response to RT (Lima et al., 2017). Furthermore, when considering the use of high RT doses (≥ 10 Gy) in a clinical setting, RT side-effects should also be taken into consideration and be accounted for in the relevant optimisation cost.

While our model captures the higher radio-resistance of CSCs, recent findings suggest that radiotherapy can directly impact the differentiation status of cells (Walcher et al., 2020). In particular, RT-induced de-differentiation has been observed *in vitro* and linked to the accumulation of senescent-type cells that can support the *de novo* formation of CSCs by influencing the tumour micro-environment. These mechanisms could be easily incorporated into our model by for example allowing the phenotypic advection velocity itself (*i.e.*, v_s) to depend on environmental factors other than oxygen. Such additions would affect the evolution of tumour heterogeneity during treatment, shifting the system into the basin of attraction of the “tumour-invasion” steady state solution. This raises the interesting question of what treatment strategies may be more effective when RT-induced RT-resistance is included and whether these may differ from the one discussed herein.

Ultimately, one can envision enlarging the cells' phenotypic state space by introducing additional “synthetic” axes that can capture more fully the cancer cells heterogeneity and evolution. However, the complexity of the model would make it difficult to gain insight into the role of the different “phenotypic” variables. Hence there is also a need to analyse simpler models, where a subset of these “synthetic” axes are included. From this point of view, given the amount of experimental evidence linking metabolism, stemness and treatment outcomes, a natural next step would be to include in the model two structure variables accounting for the stemness and metabolic status of cells. While previous theoretical studies have focused on the ways in which nutrient levels and/or treatment shape metabolic heterogeneity in tumours (e.g., Ardaševa et al., 2020; Hodgkinson et al., 2019; Villa et al., 2021), the role of stemness is yet to be investigated. A model that captures all of these aspects could provide insight into the evolution of the complex tumour ecosystem and help in the design of effective treatment strategies. While these goals are intriguing from a theoretical viewpoint, a different, but equally important, direction involves connecting phenotypic-structured model to experimental data. The development of RNA-seq techniques has resulted in a wealth of data describing the evolution of cells phenotypes (see, e.g., Patel et al., 2014). The question, then, is how these rich datasets can be used to inform phenotypic-structured models. From this point of view, important practical aspects have to be addressed, such as parameter identifiability and estimation, that can be challenging when considering highly-parameterised and computationally-expensive models. Addressing these limitations will be crucial for translating the findings of our theoretical study into clinically-relevant insight.

CRedit authorship contribution statement

Giulia L. Celora: Conceptualization, Methodology, Software, Formal analysis, Visualization, Writing – original draft, Writing – review & editing. **Helen M. Byrne:** Conceptualization, Methodology, Writing – original draft, Writing – review & editing, Supervision. **P.G. Kevrekidis:** Conceptualization, Methodology, Writing – original draft, Writing – review & editing, Supervision.

Declaration of competing interest

The authors declare that they have no known competing financial interests or personal relationships that could have appeared to influence the work reported in this paper.

Data availability

In compliance with EPSRC's open access initiative, the research materials supporting this publication can be accessed by contacting celora@maths.ox.ac.uk.

Acknowledgements

The authors thank Prof Christos E. Zois for helpful and illuminating discussions on the biology underpinning the model. G.L.C. is supported by the EPSRC and MRC funded Centre for Doctoral Training in Systems Approaches to Biomedical Science (grant number EP/L016044/1) and Cancer Research UK. G.L.C. acknowledges also the support from Worcester College via the Martin Senior Scholarships. P.G.K. acknowledges support from the Leverhulme Trust via a Visiting Fellowship and thanks the Mathematical Institute of the University of Oxford for its hospitality during the early and final stages of this work.

Appendix A. Numerical methods

Dynamical simulations. Here we describe in more detail the numerical approach used to solve Eqs. (5) and (8). We discretise the spatial variable X using central finite difference on a stencil of $(\kappa_x + 1)$ points. Ghost points are used to enforce the Neumann boundary conditions. For the phenotypic axis s , we use finite volumes dividing the s -axis into κ_s intervals of equal size. Furthermore, we control the advection component using a Koren limiter (Gerisch and Chaplain, 2006). As discussed in Celora et al. (2021), the use of a finite volume scheme allows us to account for the advective structural flux. The solution $(n(X, s, t), c(X, t))$ is therefore approximated by the vector functions $\mathbf{n}(t) \in \mathcal{R}^{(\kappa_x+1)\kappa_s}$ and $c(t) \in \mathcal{R}^{\kappa_x}$. After discretising Eqs. (5) and (8) as described, we obtain a system of $(\kappa_x + 1) \times \kappa_s$ non-linear, time-dependent ODEs of the form $\dot{\mathbf{n}}(t) = \mathbf{f}(c(t), \mathbf{n}(t), t)$ subject to κ_x non-linear algebraic constraints ($g(\mathbf{n}(t), c(t)) = 0$). Note that, given \mathbf{n} , the implicit function g uniquely defines c , i.e., we can write $c = c(\mathbf{n})$. We define $\tilde{\mathbf{f}}(\mathbf{n}, t) = \mathbf{f}(c(\mathbf{n}(t)), \mathbf{n}(t), t)$, so that the evolution of the vector function $\mathbf{n}(t)$ can be written as $\dot{\mathbf{n}}(t) = \tilde{\mathbf{f}}(\mathbf{n}(t), t)$. To advance in time, we use an implicit, adaptive multistep method based on the comparison of backward differentiation formula (Süli and Mayers, 2003) of orders 1 and 5 (i.e., *bd15*) which is designed for stiff equations. Practically the input function $\tilde{\mathbf{f}}$ for the multistep method reads

Function $\tilde{\mathbf{f}}(\mathbf{n}, t)$:

Solve for c using fixed point iterations
Assemble $\tilde{\mathbf{f}}$ using the computed oxygen distribution c
return

When including treatment, we want to properly capture the fast timescale of RT delivery. To do so, we control the maximum step allowed by the *bd15* integrator when in a neighbourhood of the time τ_i at which a RT-dose is delivered.

Numerical continuation and stability estimates. In order to compute the stationary solutions $(\bar{n}(X, s), \bar{c}(X))$ of Eqs. (5)–(6) in the absence of treatment, we set to zero all time derivatives and obtain:

$$E_n(\bar{n}, \bar{c}) = 0, \quad E_c(\bar{n}, \bar{c}) = 0, \quad E_{bc}(\bar{n}, \bar{c}) = \mathbf{e}_6, \quad (\text{A.1a})$$

where $\mathbf{e}_6 = [0, 0, 0, 0, 0, 1]^T$ and

$$E_n(n, c) = D_{xn} \frac{\partial^2 n}{\partial X^2} + \frac{\partial}{\partial s} \left(D_{sn} \frac{\partial n}{\partial s} - v_s(s, c)n \right) + F(s, c, \phi)n, \quad (\text{A.1b})$$

Table B.1

Summary of typical dimensional values for some of the parameters in Eq. (3), together with supporting references.

Parameter	Reference value(s)	Refs
D_{xn}	10^{-10} – 10^{-8} [mm ² /s]	Swanson et al. (2000), Villa et al. (2021)
$p_{DC}^{max} \tau_0^{-1}$	0.02 [1/hr]	Stone et al. (1978)
p_{CSC}^{max}	$0.25 p_{DC}^{max}$	
OER	3	Lewin et al. (2020a)
$\alpha_{min}, \Delta\alpha$	0.007, 0.143 [1/Gy]	Saga et al. (2019)
$\beta_{min}, \Delta\beta$	0.002, 0.018 [1/Gy ²]	Saga et al. (2019)
$\gamma_0 C_\infty \tau_0^{-1}$	5–50 [mmHg/s]	Grimes et al. (2014)
D_{xc}	2×10^{-3} [mm ² /s]	Grimes et al. (2014)
C_∞	50 [mmHg]	McKeown (2014), West and Slevin (2019)
C_H	15 [mmHg]	McKeown (2014), West and Slevin (2019)
C_R	5 [mmHg]	McKeown (2014), West and Slevin (2019)
C_N	≈ 0 [mmHg]	West and Slevin (2019)
L	≈ 200 [μm]	

$$E_c(n, c) = D_{xc} \frac{\partial^2 c}{\partial X^2} - \gamma^* D_{xc} \phi H_{e_\gamma}(c - c_N), \quad (\text{A.1c})$$

$$E_{bc}(n, c) = \left[\frac{\partial n}{\partial s} \Big|_{s=0}, \frac{\partial n}{\partial s} \Big|_{s=1}, \frac{\partial n}{\partial X} \Big|_{X=0}, \frac{\partial n}{\partial X} \Big|_{X=1}, \frac{\partial c}{\partial X} \Big|_{X=0}, c|_{X=1} \right]. \quad (\text{A.1d})$$

Since we cannot solve Eqs. (A.1) explicitly, we approximate \bar{n} and \bar{c} numerically. We discretise Eqs. (A.1) as described in the previous paragraph to obtain a system of $\kappa = (\kappa_x + 1) \times (\kappa_s + 1) - 1$ implicit non-linear equations: $\mathbf{G}(\bar{n}, \bar{c}) = 0$, with $\bar{n} \in \mathcal{R}^{(\kappa_x+1)\kappa_s}$ and $\bar{c} \in \mathcal{R}^{\kappa_x}$. For any fixed value of the parameters, we solve the latter using Newton's method. Bifurcation diagrams are computed numerically via numerical continuation techniques using Julia's package *BifurcationKit* (Veltz, 2020). The linear stability of the stationary solution and bifurcation points are approximated by looking at the spectrum of the Jacobian matrix $J_G \in \mathcal{R}^{\kappa \times \kappa}$, where $J_G \in \mathcal{R}^{\kappa \times \kappa} = [\nabla_n \mathbf{G}, \nabla_c \mathbf{G}]$. In particular (\bar{n}, \bar{c}) is defined as stable if $\Re(\lambda) < 0$ for all the eigenvalues λ of the matrix J_G .

Appendix B. Parameter values

We summarise here the parameter values used in the simulation of Eqs. (5)–(8) presented in the main text. In Table B.1, we list the value of dimensional parameter values that could be estimated from the literature. Most are specific to prostate cancer cell line DU 145 which is known to contain a small subpopulation of CSC-like cells (when cultured in monolayers). The proliferation rate of DCs is approximated taking the reported doubling time of 34 hr (Stone et al., 1978), i.e., $p_{DC}^{max} \tau_0^{-1} = \ln(2)/(34 \text{ h}) \approx 0.02 \text{ h}^{-1}$. The values of non-dimensional parameters are instead given in Table B.2.

Appendix C. Bifurcation analysis

C.1. Linear stability analysis of the trivial steady state

In this section, we determine the linear stability of the trivial steady state by seeking solutions of Eq. (5)–(6) of the form:

$$n(X, s, \tau) = \delta \tilde{n}(X, s) e^{\lambda \tau} + O(\delta^2), \quad c(X, \tau) = 1 + \delta \tilde{c}(X) e^{\lambda \tau} + O(\delta^2), \quad (\text{C.1})$$

where $0 < \delta \ll 1$ and $\tilde{n}, \tilde{c} \sim O(1)$. Substituting (C.1) into Eqs. (5)–(6) and retaining terms which are linear in δ we obtain the following linearised problem on $(X, s) \in (0, 1)^2$:

$$\lambda \tilde{n} = D_{xn} \frac{\partial^2 \tilde{n}}{\partial X^2} + \frac{\partial}{\partial s} \left(D_{sn} \frac{\partial \tilde{n}}{\partial s} - \tilde{n} v_s(s, 1) \right) + F(s, 1, 0) \tilde{n}, \quad (\text{C.2a})$$

$$\lambda \tilde{c} = D_{xc} \frac{\partial^2 \tilde{c}}{\partial X^2} - \gamma D_{xc} \tilde{c}, \quad (\text{C.2b})$$

Table B.2

Summary of the non-dimensional parameter groups that appear in Eq. (5)–(12). Parameter values are consistent with those reported in Table B.1 and/or in Celora et al. (2021).

Parameter	Dimensionless value(s)
D_{sn}	1.2×10^{-4}
V_+, V_-	1.92, 0.48 [$\times 10^{-3}$]
ξ_+, ξ_-	0.1, 0.1
ω_+, ω_-	1, 2
D_{xn}	2.410^{-3}
K_{CSC}, K_{DC}	0.05, 0.3
$p_{CSC}^{max}, p_{DC}^{max}$	0.12, 0.48
g_{CSC}, g_{DC}, g_{TDC}	0.1, 0.2, 0.1
d_{TDC}, d_n	0.024, 2.4
ξ_R	0.2
D_{xc}	$\approx 4.32 \times 10^3$
$\gamma_0 D_{xc}^{-1}$	2–20
c_H	0.3
c_R	0.1
c_N	0.0125

$$D_{xs} \frac{\partial \bar{n}}{\partial s} - \bar{n} v_s(s, 1) = 0, \quad s \in \{0, 1\}, X \in [0, 1], \quad (C.2c)$$

$$\frac{\partial \bar{c}}{\partial X} \Big|_{X=0} = \frac{\partial \bar{n}}{\partial X} \Big|_{X=0} = \frac{\partial \bar{n}}{\partial X} \Big|_{X=1} = 0, \quad \delta c(1, t) = 0, \quad s \in (0, 1) \quad (C.2d)$$

where $\bar{\phi}(X) = \int_0^1 \bar{n}(X, s) ds$. We note that Eq. (C.2b) for \bar{c} decouples from Eq. (C.2a). We seek separable solutions for Eq. (C.2a) of the form:

$$\bar{n}(X, s) = \Lambda(X)W(s) \quad (C.3)$$

where Λ and W satisfy:

$$\lambda = \frac{D_{xn}}{\Lambda} \frac{d^2 \Lambda}{dX^2} + \frac{1}{W} \frac{d}{ds} \left(D_{sn} \frac{dW}{ds} - v_s(s, 1)W \right) + \mathcal{P}(s, 1) - \mathcal{K}(s, 1), \quad (C.4a)$$

$$\frac{dW}{ds} \Big|_{s=0} = \frac{dW}{ds} \Big|_{s=1} = 0, \quad (C.4b)$$

$$\frac{d\Lambda}{dX} \Big|_{X=0} = \frac{d\Lambda}{dX} \Big|_{X=1} = 0. \quad (C.4c)$$

In Eq. (C.4b) we have exploited the fact that the velocity v_s vanishes at the boundaries of the phenotypic axis (i.e., $s = 0$ and $s = 1$). Using standard arguments, we find that the eigenfunctions Λ_m and eigenvalues ω_m are given by

$$\Lambda_m = \cos(\omega_m X), \quad \omega_m = \pi m, \quad m = 0, 1, 2, \dots \quad (C.5a)$$

and that the eigenfunctions W associated to the phenotypic axis, s , must satisfy the following ODE:

$$\begin{aligned} (\omega_m^2 D_{xn} + \lambda) W = \frac{d}{ds} \left(D_{sn} \frac{dW}{ds} - v_s(s, 1)W \right) \\ + [\mathcal{P}(s, 1) - \mathcal{K}(s, 1)] W \equiv \mathcal{M}(W), \end{aligned} \quad (C.5b)$$

$$D_{sn} \frac{dW}{ds} = 0, \quad s \in \{0, 1\}. \quad (C.5c)$$

Here, the operator \mathcal{M} is the differential operator obtained by linearising the well-mixed formulation of Eqs. (5), which is obtained by setting all spatial derivatives to zero and considering spatially uniform oxygen concentration. We investigated the spectrum of the operator \mathcal{M} in our previous work (Celora et al., 2021). While we do not have explicit solutions for the eigenvalues κ_k and eigenfunctions W_k of \mathcal{M} (i.e., $\mathcal{M}(W_k) = \kappa_k W_k$), we can show that κ_k are real and bounded above. Since D_{xn} is constant, then $\bar{n}_{m,k} = \Lambda_m(X)W_k(s)$ is an eigenfunction of the operator defined by Eqs. (C.4), with real growth rate $\lambda_{m,k} = \kappa_k - \omega_m^2 D_{xn}$. Since $\omega^2 D_{xn} \geq 0$, we find that $\lambda_{m,k} \leq \kappa_k$ and $\lambda_{m,k} < \lambda_{m',k}$ if $m' < m$. Consequently, $\lambda_{m,k} < 0$ for all k and m if and only if $\bar{\kappa} = \max_k \kappa_k < 0$.

The question now is whether $\lambda = \bar{\kappa}$ is an eigenvalue for the full system Eqs. (C.2). If this is the case, then the stability of the trivial steady-state for the model Eqs. (5)–(6) reduces to studying the linear stability of the steady state for the well-mixed model for homogeneous

oxygen concentration $c \equiv 1$. Let us consider the case $\omega_m \equiv 0$ for which $\text{wlog } \Lambda_0 \equiv 1$. In this case, the eigenfunction associated with the eigenvalue $\bar{\kappa}$ is $\bar{n} = W_{\bar{\kappa}}(s)$. The eigenfunction is defined up to a multiplicative constant which we fix so that $\int_0^1 W_k(s) ds = \bar{\phi} \equiv \Delta > 0$. If $\bar{\kappa}$ is an eigenvalue of Eqs. (C.2), then Eq. (C.2b) must have a solution with $\lambda = \bar{\kappa}$ and $\bar{\phi} \equiv \Delta$. Substituting for λ and $\bar{\phi}$, we obtain:

$$\bar{\kappa} \bar{c}_{\bar{\kappa}} + \gamma_0 \Delta = D_{xc} \frac{\partial^2 \bar{c}_{\bar{\kappa}}}{\partial X^2}, \quad (C.6a)$$

$$\bar{c}_{\bar{\kappa}}(1) = 0, \quad \partial_x \bar{c}_{\bar{\kappa}}(0) = 0, \quad (C.6b)$$

which has the solution:

$$\bar{c}_{\bar{\kappa}}(X) = \begin{cases} \frac{\gamma_0 \Delta}{\bar{\kappa}} \left[\frac{\cosh(\ell X)}{\cosh(\ell)} - 1 \right], & \bar{\kappa} > 0, \\ \frac{\gamma_0 \Delta}{2D_{xc}} (X^2 - 2), & \bar{\kappa} = 0, \\ \frac{\gamma_0 \Delta}{\bar{\kappa}} \left[\frac{\cos(\ell X)}{\cos(\ell)} - 1 \right], & \bar{\kappa} < 0, \end{cases} \quad (C.6c)$$

where $\ell = \sqrt{|\bar{\kappa}/D_{xc}|}$. Given that a solution exists, we have that $\bar{\kappa}$ belongs to the spectrum of the full operator, Eqs. (C.2), with eigenfunction $(W_{\bar{\kappa}}(s), \bar{c}_{\bar{\kappa}}(X))$. Further, since the spectrum of Eqs. (C.2) is a subset of $\lambda_{m,k} \leq \bar{\kappa}$, $\bar{\kappa}$ will be the eigenvalue with largest real part and therefore dictates the stability of the trivial solution. From Celora et al. (2021), we know that $\bar{\kappa}$ decreases from positive to negative values as the magnitude of the advection velocity V_+ increases. The critical value $V_+^{(cr)}$ at which $\bar{\kappa} = 0$, corresponds to a transcritical bifurcation. Therefore this bifurcation must occur also in the spatial model, and, based on the above result, the location of the transcritical bifurcation $V_+ = V_+^{(cr)}$ is independent of γ_0 , D_{xn} and D_{xc} . We conclude that the critical value $V_+^{(cr)}$ at which the transcritical bifurcation occurs will not be affected by the inclusion of spatial effects, in line with the numerical bifurcation diagrams presented in the main text.

C.2. Additional figures

In Section 4 in the main text, we set the maximum proliferation rate \bar{p} (with $p_{DC}^{max} = \bar{p}$ and $p_{CSC}^{max} = 0.25\bar{p}$) to $\bar{p} = 0.48$. As mentioned the qualitative bifurcation structure of the model does not change when we vary \bar{p} (at least in the range considered in Fig. 10). For completeness, we compute the bifurcation diagram in Fig. 12 but setting $\bar{p} = 0.24$. This is illustrated in Fig. C.21. Comparing Fig. C.21 with Fig. 12, we see that the parameter space is divided into the same five regions by the trajectories of the fold points (in red) and the transcritical bifurcation point (in yellow). As we have shown in Fig. 9, the location of the transcritical point ($V_+ = V_+^{(cr)}$) decreases with \bar{p} ; similarly the location of the cusp point is shifted towards smaller value of V_+ , while the γ_0 coordinate remains barely affected.

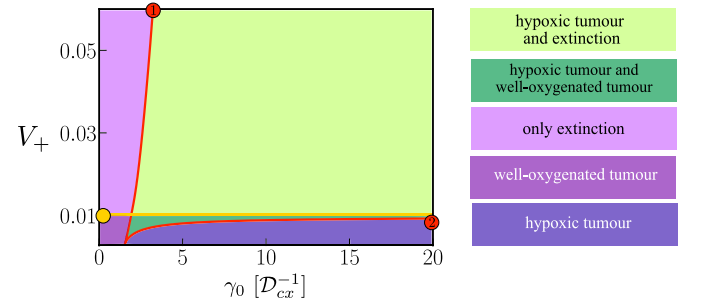


Fig. C.21. Continuation of the fold points SN_1 and SN_2 in the (γ_0, V_+) parameter space for $\bar{p} = 0.24$. Here SN_1 and SN_2 are as identified in the bifurcation diagrams in Figs. 11. The points SN_1 and SN_2 divide the parameter spaces in regions where Eqs. (A.1) admits a different number of solutions (as indicated by the different colours). The two saddle nodes originates from a cusp point.

References

- Anderson, A.R.A., Chaplain, M.A.J., 1998. Continuous and discrete mathematical models of tumor-induced angiogenesis. *Bull. Math. Biol.* 60 (5), 857–899. <http://dx.doi.org/10.1006/bulm.1998.0042>.
- Aponte, P.M., Caicedo, A., 2017. Stemness in cancer: Stem cells, cancer stem cells, and their microenvironment. *Stem Cells Int.* 2017, <http://dx.doi.org/10.1155/2017/5619472>.
- Ardaševa, A., Gatenby, R.A., Anderson, A.R.A., Byrne, H.M., Maini, P.K., Lorenzi, T., 2020. A mathematical dissection of the adaptation of cell populations to fluctuating oxygen levels. *Bull. Math. Biol.* 82 (6), 1–24. <http://dx.doi.org/10.1007/S11538-020-00754-7>.
- Arnold, C.R., Mangesius, J., Skvortsova, I.-I., Ganswindt, U., 2020. The role of cancer stem cells in radiation resistance. *Front. Oncol.* 10, 164. <http://dx.doi.org/10.3389/FONC.2020.00164>.
- Ashton, T.M., Fokas, E., Kunz-Schughart, L.A., Folkes, L.K., Anbalagan, S., Huether, M., Kelly, C.J., Pirovano, G., Buffa, F.M., Hammond, E.M., Stratford, M., Muschel, R.J., Higgins, G.S., McKenna, W.G., 2016. The anti-malarial atovaquone increases radiosensitivity by alleviating tumour hypoxia. *Nature Commun.* 7 (1), 1–13. <http://dx.doi.org/10.1038/ncomms12308>.
- Astanin, S., Preziosi, L., 2009. Mathematical modelling of the warburg effect in tumour cords. *J. Theoret. Biol.* 258 (4), 578–590. <http://dx.doi.org/10.1016/J.JTBI.2009.01.034>.
- Axelsson, H., Fredlund, E., Ovenberger, M., Landberg, G., Pålman, S., 2005. Hypoxia-induced dedifferentiation of tumor cells – a mechanism behind heterogeneity and aggressiveness of solid tumors. *Sem. Cell Develop. Biol.* 16 (4–5), 554–563. <http://dx.doi.org/10.1016/J.SEMCDB.2005.03.007>.
- Bacevic, K., Noble, R., Soffar, A., Ammar, O.W., Boszonyik, B., Prieto, S., Vincent, C., Hochberg, M.E., Krasinska, L., Fisher, D., 2017. Spatial competition constrains resistance to targeted cancer therapy. *Nat. Commun.* 8 (1), 1–15. <http://dx.doi.org/10.1038/s41467-017-01516-1>.
- Baliu-Piqué, M., Pandiella, A., Ocana, A., 2020. Breast cancer heterogeneity and response to novel therapeutics. *Cancers* 12 (11), 1–16. <http://dx.doi.org/10.3390/CANCERS12113271>.
- Barendsen, G., 1982. Dose fractionation, dose rate and iso-effect relationships for normal tissue responses. *Int. J. Radiat. Oncol. Biol. Phys.* 8 (11), 1981–1997. [http://dx.doi.org/10.1016/0360-3016\(82\)90459-X](http://dx.doi.org/10.1016/0360-3016(82)90459-X).
- Barendsen, G.W., Van Bree, C., Franken, N.A., 2001. Importance of cell proliferative state and potentially lethal damage repair on radiation effectiveness: Implications for combined tumor treatments (review). *Int. J. Oncol.* 19 (2), 247–256. <http://dx.doi.org/10.3892/IJO.19.2.247>.
- Black, J.R.M., McGranahan, N., 2021. Genetic and non-genetic clonal diversity in cancer evolution. *Nat. Rev. Cancer* 1–14. <http://dx.doi.org/10.1038/s41568-021-00336-2>.
- Brüningk, S., Powathil, G., Ziegenhein, P., Ijaz, J., Rivens, I., Nill, S., Chaplain, M., Oelfke, U., Haar, G.T., 2018. Combining radiation with hyperthermia: a multiscale model informed by in vitro experiments. *J. R. Soc. Interface* 15, <http://dx.doi.org/10.1098/RSIF.2017.0681>.
- Bull, J.A., Mech, F., Quaiser, T., Waters, S.L., Byrne, H.M., 2020. Mathematical modelling reveals cellular dynamics within tumour spheroids. *PLoS Comput. Biol.* 16 (8), e1007961. <http://dx.doi.org/10.1371/JOURNAL.PCBI.1007961>.
- Byrne, H., Preziosi, L., 2003. Modelling solid tumour growth using the theory of mixtures. *Math. Med. Biol.* 20, 341–366. <http://dx.doi.org/10.1093/imammb/20.4.341>.
- Cajal, S.R.y., Sesé, M., Capdevila, C., Aasen, T., Mattos-Arruda, L.D., Diaz-Cano, S.J., Hernández-Losa, J., Castellví, J., 2020. Clinical implications of intratumor heterogeneity: challenges and opportunities. *J. Mole. Med.* 98 (2), 161. <http://dx.doi.org/10.1007/S00109-020-01874-2>.
- Celora, G., Byrne, H., Zois, C., Kevrekidis, P., 2021. Phenotypic variation modulates the growth dynamics and response to radiotherapy of solid tumours under normoxia and hypoxia. *J. Theoret. Biol.* 110792. <http://dx.doi.org/10.1016/j.jtbi.2021.110792>.
- Chae, Y.C., Kim, J.H., 2018. Cancer stem cell metabolism: target for cancer therapy. *BMB Rep.* 51 (7), 319. <http://dx.doi.org/10.5483/BMBREP.2018.51.7.112>.
- Chisholm, R., Lorenzi, T., Clairambault, J., 2016. Cell population heterogeneity and evolution towards drug resistance in cancer: Biological and mathematical assessment, theoretical treatment optimisation. *Biochim. Biophys. Acta* 1860 (11), 2627–2645. <http://dx.doi.org/10.1016/j.bbagen.2016.06.009>.
- Chisholm, R.H., Lorenzi, T., Lorz, A., et al., 2015. Emergence of drug tolerance in cancer cell populations: An evolutionary outcome of selection, nongenetic instability, and stress-induced adaptation. *Cancer Res.* 75 (6), 930–939. <http://dx.doi.org/10.1158/0008-5472.CAN-14-2103>.
- Cohen, D.S., Murray, J.D., 1981. A generalized diffusion model for growth and dispersal in a population. *J. Math. Biol.* 12 (2), 237–249. <http://dx.doi.org/10.1007/BF00276132>.
- Dagogo-Jack, I., Shaw, A.T., 2018. Tumour heterogeneity and resistance to cancer therapies. *Nat. Rev. Clin. Oncol.* 15 (2), 81–94. <http://dx.doi.org/10.1038/nrclinonc.2017.166>.
- Damaghi, M., West, J., Robertson-Tessi, M., Xu, L., Ferrall-Fairbanks, M.C., Stewart, P.A., Persi, E., Fridley, B.L., Altmock, P.M., Gatenby, R.A., Sims, P.A., Anderson, A.R.A., Gillies, R.J., 2021. The harsh microenvironment in early breast cancer selects for a warburg phenotype. *Proc. Natl. Acad. Sci.* 118 (3), <http://dx.doi.org/10.1073/PNAS.2011342118>.
- De Thé, H., 2017. Differentiation therapy revisited. *Nat. Rev. Cancer* 18 (2), 117–127. <http://dx.doi.org/10.1038/nrc.2017.103>.
- Dearmaley, D., Syndikus, I., Mossop, H., Khoo, V., Birtle, A., Bloomfield, D., Graham, J., Kirkbride, P., Logue, J., Malik, Z., Money-Kyrle, J., O'Sullivan, J.M., Panades, M., Parker, C., Patterson, H., Scrase, C., Staffurth, J., Stockdale, A., Tremlett, J., Bidmead, M., Mayles, H., Naismith, O., South, C., Gao, A., Cruickshank, C., Hassan, S., Pugh, J., Griffin, C., Hall, E., 2016. Conventional versus hypofractionated high-dose intensity-modulated radiotherapy for prostate cancer: 5-year outcomes of the randomised, non-inferiority, phase 3 CHHiP trial. *Lancet Oncol.* 17, 1047–1060. [http://dx.doi.org/10.1016/S1470-2045\(16\)30102-4/ATTACHMENT/A874D557-6CC5-4170-A0F0-E5C7B74D427A/MMC1.PDF](http://dx.doi.org/10.1016/S1470-2045(16)30102-4/ATTACHMENT/A874D557-6CC5-4170-A0F0-E5C7B74D427A/MMC1.PDF).
- Dhawan, A., Tonekaboni, S.A.M., Taube, J.H., Hu, S., Sphyrin, N., Mani, S.A., Kohandel, M., 2016. Mathematical modelling of phenotypic plasticity and conversion to a stem-cell state under hypoxia. *Sci. Rep.* 6 (1), 1–10. <http://dx.doi.org/10.1038/srep18074>.
- Diehn, M., Cho, R.W., Lobo, N.A., Kalisky, T., Dorie, M.J., Kulp, A.N., Qian, D., Lam, J.S., Ailles, L.E., Wong, M., Joshua, B., Kaplan, M.J., Wapnir, I., Dirbas, F.M., Somlo, G., Garberoglio, C., Paz, B., Shen, J., Lau, S.K., Quake, S.R., Brown, J.M., Weissman, I.L., Clarke, M.F., 2009. Association of reactive oxygen species levels and radioresistance in cancer stem cells. *Nature* 458 (7239), 780–783. <http://dx.doi.org/10.1038/nature07733>.
- Enderling, H., Park, D., Hlatky, L., Hahnfeldt, P., 2009. The importance of spatial distribution of stemness and proliferation state in determining tumor radioresponse. *Math. Model. Nat. Phenom.* 4 (3), 117–133. <http://dx.doi.org/10.1051/MMNP/20094305>.
- Fanelli, G.N., Naccarato, A.G., Scatena, C., 2020. Recent advances in cancer plasticity: Cellular mechanisms, surveillance strategies, and therapeutic optimization. *Front. Oncol.* 10, 569. <http://dx.doi.org/10.3389/fonc.2020.00569>.
- Fiandaca, G., Delitala, M., Lorenzi, T., 2021. A mathematical study of the influence of hypoxia and acidity on the evolutionary dynamics of cancer. *Bull. Math. Biol.* 83 (7), 1–29. <http://dx.doi.org/10.1007/S11538-021-00914-3>.
- Fiorillo, M., Lamb, R., Tanowitz, H.B., Mutti, L., Krstic-Demonacos, M., Cappello, A.R., Martinez-Outschoorn, U.E., Sotgia, F., Lisanti, M.P., 2016. Repurposing atovaquone: Targeting mitochondrial complex III and oxphos to eradicate cancer stem cells. *Oncotarget* 7 (23), 34084–34099. <http://dx.doi.org/10.18632/oncotarget.9122>.
- Fowler, J.F., 1989. The linear-quadratic formula and progress in fractionated radiotherapy. *Brit. J. Radiol.* 62 (740), 679–694. <http://dx.doi.org/10.1259/0007-1285-62-740-679>.
- Franken, N.A., Oei, A.L., Kok, H.P., Rodermond, H.M., Sminia, P., Crezee, J., Stalpers, L.J., Barendsen, G.W., 2013. Cell survival and radiosensitisation: modulation of the linear and quadratic parameters of the LQ model (review). *Int. J. Oncol.* 42 (5), 1501–1515. <http://dx.doi.org/10.3892/IJO.2013.1857>.
- Frieboes, H.B., Jin, F., Chuang, Y.L., Wise, S.M., Lowengrub, J.S., V, V.C., 2010. Three-dimensional multispecies nonlinear tumor growth—II: Tumor invasion and angiogenesis. *J. Theoret. Biol.* 264, 1254–1278. <http://dx.doi.org/10.1016/J.JTBI.2010.02.036>.
- Gad, S., 2014. Maximum tolerated dose. In: Wexler, P. (Ed.), *Encyclopedia of Toxicology*, third ed. Academic Press, Oxford, p. 164. <http://dx.doi.org/10.1016/B978-0-12-386454-3.00874-5>.
- Galez, C., Totis, C., Bisio, A., 2021. Radiation resistance: A matter of transcription factors. *Front. Oncol.* 2025. <http://dx.doi.org/10.3389/FONC.2021.662840>.
- Garnier, D., Renoult, O., Alves-Guerra, M.C., Paris, F., Pecqueur, C., 2019. Glioblastoma stem-like cells, metabolic strategy to kill a challenging target. *Front. Oncol.* 9 (MAR), 118. <http://dx.doi.org/10.3389/fonc.2019.00118>.
- Gerisch, A., Chaplain, M.A., 2006. Robust numerical methods for taxis-diffusion-reaction systems: Applications to biomedical problems. *Math. Comput. Modelling* 43 (1–2), 49–75. <http://dx.doi.org/10.1016/j.mcm.2004.05.016>.
- Greaves, M., Maley, C.C., 2012. Clonal evolution in cancer. *Nature* 481 (7381), 306–313. <http://dx.doi.org/10.1038/nature10762>.
- Greenspan, H.P., 1972. Models for the growth of a solid tumor by diffusion. *Stud. Appl. Math.* 51 (4), 317–340. <http://dx.doi.org/10.1002/sapm1972514317>.
- Grimes, D.R., Fletcher, A.G., Partridge, M., 2014. Oxygen consumption dynamics in steady-state tumour models. *Roy. Soc. Open Sci.* 1 (1), 140080. <http://dx.doi.org/10.1098/rsos.140080>.
- Hanahan, D., Weinberg, R.A., 2000. The hallmarks of cancer. *Cell* 100 (1), 57–70. [http://dx.doi.org/10.1016/S0092-8674\(00\)81683-9](http://dx.doi.org/10.1016/S0092-8674(00)81683-9).
- Heddleston, J.M., Li, Z., Lathia, J.D., Bao, S., Hjelmeland, A.B., Rich, J.N., 2010. Hypoxia inducible factors in cancer stem cells. *Brit. J. Cancer* 102 (5), 789–795. <http://dx.doi.org/10.1038/sj.bjc.6605551>.
- Höckel, M., Vaupel, P., 2001. Tumor hypoxia: Definitions and current clinical, biologic, and molecular aspects. *JNCI: J. Natl Cancer Instit.* 93 (4), 266–276. <http://dx.doi.org/10.1093/jnci/93.4.266>.
- Hodgkinson, A., Le Cam, L., Trucu, D., et al., 2019. Spatio-genetic and phenotypic modelling elucidates resistance and re-sensitisation to treatment in heterogeneous melanoma. *J. Theoret. Biol.* 466, 84–105. <http://dx.doi.org/10.1016/j.jtbi.2018.11.037>.

- Hoffmann, M., Chang, H.H., Huang, S., Ingber, D.E., Loeffler, M., Galle, J., 2008. Noise-driven stem cell and progenitor population dynamics. *PLOS ONE* 3 (8), e2922. <http://dx.doi.org/10.1371/JOURNAL.PONE.0002922>.
- Hubbard, M.E., Byrne, H.M., 2013. Multiphase modelling of vascular tumour growth in two spatial dimensions. *J. Theoret. Biol.* 316, 70–89. <http://dx.doi.org/10.1016/j.jtbi.2012.09.031>.
- Jones, B., Dale, R., Deehan, C., Hopkins, K., Morgan, D., 2001. The role of biologically effective dose (BED) in clinical oncology. *Clin. Oncol.* 13 (2), 71–81. <http://dx.doi.org/10.1053/clon.2001.9221>.
- Kainuma, T., Kawakami, S., Tsumura, H., Satoh, T., Tabata, K.I., Iwamura, M., Hayakawa, K., Ishiyama, H., 2019. A phase I dose-escalation trial of stereotactic body radiotherapy using 4 fractions for patients with localized prostate cancer. *Radiat. Oncol.* 14, 1–6. <http://dx.doi.org/10.1186/S13014-019-1369-Y/TABLES/6>.
- Koh, M.Y., Lemos, R., Liu, X., Powis, G., 2011. The hypoxia-associated factor switches cells from HIF-1 α - to HIF-2 α -dependent signaling promoting stem cell characteristics, aggressive tumor growth and invasion. *Cancer Res.* 71 (11), 4015–4027. <http://dx.doi.org/10.1158/0008-5472.CAN-10-4142>.
- Lewin, T.D., Byrne, H.M., Maini, P.K., Caudell, J.J., Moros, E.G., Enderling, H., 2020a. The importance of dead material within a tumour on the dynamics in response to radiotherapy. *Phys. Med. Biol.* 65 (1), 015007. <http://dx.doi.org/10.1088/1361-6560/ab4c27>.
- Lewin, T.D., Maini, P.K., Moros, E.G., Enderling, H., Byrne, H.M., 2020b. A three phase model to investigate the effects of dead material on the growth of avascular tumours. *Math. Model. Nat. Phenom.* 15, 22. <http://dx.doi.org/10.1051/mmnp/2019039>.
- Lima, E.A., Oden, J.T., Wohlmuth, B., Shahmoradi, A., Hormuth, D.A., Yankeelov, T.E., Scarabosio, L., Horger, T., 2017. Selection and validation of predictive models of radiation effects on tumor growth based on noninvasive imaging data. *Comput. Methods Appl. Mech. Engrg.* 327, 277–305. <http://dx.doi.org/10.1016/J.CMA.2017.08.009>.
- Lorenzi, T., Chisholm, R., Clairambault, J., 2016. Tracking the evolution of cancer cell populations through the mathematical lens of phenotype-structured equations. *Biology Direct* 11 (1), 43. <http://dx.doi.org/10.1186/s13062-016-0143-4>.
- Lorenzi, T., Venkataraman, C., Lorz, A., Chaplain, M.A., 2018. The role of spatial variations of abiotic factors in mediating intratumour phenotypic heterogeneity. *J. Theoret. Biol.* 451, 101–110. <http://dx.doi.org/10.1016/J.JTBL.2018.05.002>.
- Lorz, A., Lorenzi, T., Clairambault, J., et al., 2015. Modeling the effects of space structure and combination therapies on phenotypic heterogeneity and drug resistance in solid tumours. *Bull. Math. Biol.* 77 (1), 1–22. <http://dx.doi.org/10.1007/s11538-014-0046-4>.
- Marusyk, A., Almendro, V., Polyak, K., 2012. Intra-tumour heterogeneity: A looking glass for cancer? *Nat. Rev. Cancer* 12 (5), 323–334. <http://dx.doi.org/10.1038/nrc3261>.
- Marusyk, A., Janiszewska, M., Polyak, K., 2020. Intratumour heterogeneity: The rosetta stone of therapy resistance. *Cancer Cell* 37 (4), 471–484. <http://dx.doi.org/10.1016/J.CCELL.2020.03.007>.
- McKeown, S.R., 2014. Defining normoxia, physoxia and hypoxia in tumours—implications for treatment response. *Brit. J. Radiol.* 87 (1035), 20130676. <http://dx.doi.org/10.1259/bjr.20130676>, PMID: 24588669.
- McMahon, S.J., 2018. The linear quadratic model: usage, interpretation and challenges. *Phys. Med. Biol.* 64 (1), 01TR01. <http://dx.doi.org/10.1088/1361-6560/AAF26A>.
- Mudassar, F., Shen, H., O'Neill, G., Hau, E., 2020. Targeting tumor hypoxia and mitochondrial metabolism with anti-parasitic drugs to improve radiation response in high-grade gliomas. *J. Exp. Clin. Cancer Res.* 39 (1), 208. <http://dx.doi.org/10.1186/s13046-020-01724-6>.
- Najafi, M., Mortezaee, K., Majidpoor, J., 2019. Cancer stem cell (CSC) resistance drivers. *Life Sci.* 234, 116781. <http://dx.doi.org/10.1016/J.LFS.2019.116781>.
- Noble, R., Burri, D., Le Sueur, C., Lemant, J., Viostat, Y., Kather, J.N., Beerwinkel, N., 2021. Spatial structure governs the mode of tumour evolution. *Nat. Ecol. Evol* 6 (2), 207–217. <http://dx.doi.org/10.1038/s41559-021-01615-9>.
- Olivares-Urbano, M.A., Griñán-Lisón, C., Marchal, J.A., Núñez, M.I., 2020. CSC radioresistance: A therapeutic challenge to improve radiotherapy effectiveness in cancer. *Cells* 9 (7), 1651. <http://dx.doi.org/10.3390/cells9071651>.
- Patel, A.P., Tirosh, I., Trombetta, J.J., Shalek, A.K., Gillespie, S.M., Wakimoto, H., Cahill, D.P., Nahed, B.V., Curry, W.T., Martuza, R.L., Louis, D.N., Rozenblatt-Rosen, O., Suvà, M.L., Regev, A., Bernstein, B.E., 2014. Single-cell RNA-seq highlights intratumoral heterogeneity in primary glioblastoma. *Science* 344 (6190), 1396–1401. <http://dx.doi.org/10.1126/science.1254257>.
- Petrova, V., Annicchiarico-Petruzzelli, M., Melino, G., Amelio, I., 2018. The hypoxic tumour microenvironment. *Oncogenesis* 7 (1), 1–13. <http://dx.doi.org/10.1038/s41389-017-0011-9>.
- Phillips, C.M., Lima, E.A., Woodall, R.T., Brock, A., Yankeelov, T.E., 2020. A hybrid model of tumor growth and angiogenesis: In silico experiments. *PLOS ONE* 15, e0231137. <http://dx.doi.org/10.1371/JOURNAL.PONE.0231137>.
- Picco, N., Gatenby, R.A., Anderson, A.R., 2017. Stem cell plasticity and niche dynamics in cancer progression. *IEEE Trans. Biomed. Eng.* 64 (3), 528–537. <http://dx.doi.org/10.1109/TBME.2016.2607183>.
- Pisco, A.O., Huang, S., 2015. Non-genetic cancer cell plasticity and therapy-induced stemness in tumour relapse: ‘what does not kill me strengthens me’. *Br. J. Cancer* 112 (11), 1725–1732. <http://dx.doi.org/10.1038/bjc.2015.146>.
- Pouchol, C., Clairambault, J., Lorz, A., Trélat, E., 2018. Asymptotic analysis and optimal control of an integro-differential system modelling healthy and cancer cells exposed to chemotherapy. *J. Math. Pures Appl.* 116, 268–308. <http://dx.doi.org/10.1016/J.MATPUR.2017.10.007>.
- Rockne, R., Alvord, E.C., Rockhill, J.K., Swanson, K.R., 2008. A mathematical model for brain tumor response to radiation therapy. *J. Math. Biol.* 58, 561–578. <http://dx.doi.org/10.1007/S00285-008-0219-6>.
- Ruan, K., Song, G., Ouyang, G., 2009. Role of hypoxia in the hallmarks of human cancer. *J. Cellular Biochem.* 107 (6), 1053–1062. <http://dx.doi.org/10.1002/JCB.22214>.
- Saga, R., Matsuya, Y., Takahashi, R., et al., 2019. Analysis of the high-dose-range radioresistance of prostate cancer cells, including cancer stem cells, based on a stochastic model. *J. Radiat. Res.* 60 (3), 298–307. <http://dx.doi.org/10.1093/jrr/rrz011>.
- Scott, J.G., Hjelmeland, A.B., Chinnaiyan, P., Anderson, A.R.A., Basanta, D., 2014. Microenvironmental variables must influence intrinsic phenotypic parameters of cancer stem cells to affect tumourigenicity. *PLoS Comput. Biol.* 10 (1), e1003433. <http://dx.doi.org/10.1371/JOURNAL.PCBI.1003433>.
- Shen, S., Clairambault, J., 2020. Cell plasticity in cancer cell populations. *F1000Research* 9, <http://dx.doi.org/10.12688/f1000research.24803.1>.
- Sia, J., Szmyd, R., Hau, E., Gee, H.E., 2020. Molecular mechanisms of radiation-induced cancer cell death: A primer. *Front. Cell Develop. Biol.* 8, <http://dx.doi.org/10.3389/fcell.2020.00041>.
- Snyder, V., Reed-Newman, T.C., Arnold, L., Thomas, S.M., Anant, S., 2018. Cancer stem cell metabolism and potential therapeutic targets. *Front. Oncol.* 8 (JUN), <http://dx.doi.org/10.3389/fonc.2018.00203>.
- Sørensen, B.S., Horsman, M.R., 2020. Tumor hypoxia: Impact on radiation therapy and molecular pathways. *Front. Oncol.* 10, 562. <http://dx.doi.org/10.3389/FONC.2020.00562>.
- Sousa, B., Ribeiro, A.S., Paredes, J., 2019. Heterogeneity and plasticity of breast cancer stem cells. *Adv. Exp. Med. Biol.* 1139, 83–103. http://dx.doi.org/10.1007/978-3-030-14366-4_5.
- Stace, R.E., Stiehl, T., Chaplain, M.A., Marciniak-Czochra, A., Lorenzi, T., 2020. Discrete and continuum phenotype-structured models for the evolution of cancer cell populations under chemotherapy. *Math. Model. Nat. Phenom.* 15, 14. <http://dx.doi.org/10.1051/MMNP/2019027>.
- Stone, K.R., Mickey, D.D., Wunderli, H., Mickey, G.H., Paulson, D.F., 1978. Isolation of a human prostate carcinoma cell line (DU 145). *Int. J. Cancer* 21 (3), 274–281. <http://dx.doi.org/10.1002/ijc.2910210305>.
- Strobl, M.A.R., Gallaher, J., West, J., Robertson-Tessi, M., Maini, P.K., Anderson, A.R.A., 2022. Spatial structure impacts adaptive therapy by shaping intra-tumoral competition. *Commun. Med* 2 (1), 1–18. <http://dx.doi.org/10.1038/s43856-022-00110-x>.
- Süli, E., Mayers, D.F., 2003. *An Introduction To Numerical Analysis*. Cambridge University Press, <http://dx.doi.org/10.1017/CBO9780511801181>.
- Suwa, T., Kobayashi, M., Nam, J.-M., Harada, H., 2021. Tumor microenvironment and radioresistance. *Exp. Mole. Med.* 53 (6), 1029–1035. <http://dx.doi.org/10.1038/s12276-021-00640-9>.
- Swanson, K.R., Alvord Jr., E.C., Murray, J.D., 2000. A quantitative model for differential motility of gliomas in grey and white matter. *Cell Prolifer.* 33 (5), 317–329. <http://dx.doi.org/10.1046/j.1365-2184.2000.00177.x>.
- Syljuåsen, R.G., 2019. Cell cycle effects in radiation oncology. In: Wenz, F. (Ed.), *Radiation Oncology*. Springer International Publishing, pp. 1–8. http://dx.doi.org/10.1007/978-3-319-52619-5_101-1.
- Tang, L., Wei, F., Wu, Y., He, Y., Shi, L., Xiong, F., Gong, Z., Guo, C., Li, X., Deng, H., Cao, K., Zhou, M., Xiang, B., Li, X., Li, Y., Li, G., Xiong, W., Zeng, Z., 2018. Role of metabolism in cancer cell radioresistance and radiosensitization methods. *J. Exp. Clin. Cancer Res.* 37 (1), <http://dx.doi.org/10.1186/S13046-018-0758-7>.
- Vavourakis, V., Wijeratne, P.A., Shipley, R., Loizidou, M., Stylianopoulos, T., Hawkes, D.J., 2017. A validated multiscale in-silico model for mechano-sensitive tumour angiogenesis and growth. *PLoS Comput. Biol.* 13, e1005259. <http://dx.doi.org/10.1371/JOURNAL.PCBI.1005259>.
- Veltz, R., 2020. BifurcationKit.jl. Inria Sophia-Antipolis, URL <https://hal.archives-ouvertes.fr/hal-02902346>.

- Villa, C., Chaplain, M.A.J., Lorenzi, T., 2020. Evolutionary dynamics in vascularised tumours under chemotherapy: Mathematical modelling, asymptotic analysis and numerical simulations. *Vietnam J. Math.* 49 (1), 143–167. <http://dx.doi.org/10.1007/S10013-020-00445-9>.
- Villa, C., Chaplain, M.A., Lorenzi, T., 2021. Modeling the emergence of phenotypic heterogeneity in vascularized tumors. *SIAM J. Appl. Math.* 81 (2), 434–453. <http://dx.doi.org/10.1137/19M1293971>.
- Walcher, L., Kistenmacher, A.-K., Suo, H., Kitte, R., Dluczek, S., Strauß, A., Bładyszun, A.-R., Yevsa, T., Fricke, S., Kossatz-Boehlert, U., 2020. Cancer stem cells—Origins and biomarkers: Perspectives for targeted personalized therapies. *Front. Immunol.* 11, 1280. <http://dx.doi.org/10.3389/fimmu.2020.01280>.
- Wenzl, T., Wilkens, J.J., 2011. Theoretical analysis of the dose dependence of the oxygen enhancement ratio and its relevance for clinical applications. *Radiat. Oncol.* 6 (1), 1–9. <http://dx.doi.org/10.1186/1748-717X-6-171>.
- West, C.M., Slevin, F., 2019. Tumour hypoxia. *Clin. Oncol.* 31 (9), 595–599. <http://dx.doi.org/10.1016/j.clon.2019.06.008>.